

Weierstraß-Institut
für Angewandte Analysis und Stochastik
Leibniz-Institut im Forschungsverbund Berlin e. V.

Preprint

ISSN 2198-5855

Stability of spiral chimera states on a torus

Oleh E. Omel'chenko¹, Matthias Wolfrum¹, Edgar Knobloch²

submitted: August 25, 2017

¹ Weierstrass Institute

Mohrenstr. 39

10117 Berlin

Germany

E-Mail: oleh.omelchenko@wias-berlin.de

matthias.wolfrum@wias-berlin.de

² Department of Physics

University of California

Berkeley, CA 94720

USA

E-Mail: knobloch@berkeley.edu

No. 2417

Berlin 2017



2010 *Mathematics Subject Classification.* 34C15, 37G35, 34D06, 35B36.

Key words and phrases. Coupled oscillators, coherence-incoherence patterns, chimera states, Ott–Antonsen equation, bifurcation analysis.

The work of OO and MW was supported by the DFG within the framework of Collaborative Research Center SFB 910. The work of EK was supported in part by the National Science Foundation under grant DMS-1613132.

Edited by
Weierstraß-Institut für Angewandte Analysis und Stochastik (WIAS)
Leibniz-Institut im Forschungsverbund Berlin e. V.
Mohrenstraße 39
10117 Berlin
Germany

Fax: +49 30 20372-303
E-Mail: preprint@wias-berlin.de
World Wide Web: <http://www.wias-berlin.de/>

Stability of spiral chimera states on a torus

Oleh E. Omel'chenko, Matthias Wolfrum, Edgar Knobloch

Abstract

We study destabilization mechanisms of spiral coherence-incoherence patterns known as spiral chimera states that form on a two-dimensional lattice of nonlocally coupled phase oscillators. For this purpose we employ the linearization of the Ott–Antonsen equation that is valid in the continuum limit and perform a detailed two-parameter stability analysis of a D_4 -symmetric chimera state, i.e., a four-core spiral state. We identify fold, Hopf and parity-breaking bifurcations as the main mechanisms whereby spiral chimeras can lose stability. Beyond these bifurcations we find new spatio-temporal patterns, in particular, quasiperiodic chimeras, D_2 -symmetric spiral chimeras as well as drifting states.

1 Introduction

Self-organization or spontaneous pattern formation is a fundamental property of spatially extended nonlinear systems. The pioneering work of A. Turing led to increased interest in the emergence of various types of patterns and their stability properties. This paper is devoted to a study of self-organized patterns of coherence and incoherence, called *chimera states*, that are present, under appropriate conditions, in discrete media. In a continuum limit these patterns appear as relative equilibria but their properties can differ from those of classical patterns in continuous media, such as reaction-diffusion systems. In this paper, we investigate spiral chimera states [8, 26], which are found in two-dimensional lattices of coupled phase oscillators. A spiral chimera consists of a coherent outer region resembling the usual spiral wave familiar from reaction-diffusion systems, and an incoherent inner core that masks the position of the phase defect. Spiral chimeras were discovered almost simultaneously with the simpler and far better studied one-dimensional chimera states [7, 1, 24], but up to now their properties have received much less attention.

Numerical simulations of coupled oscillator systems reveal that spiral chimeras can be found on two-dimensional lattices with periodic [6, 17, 3, 29] as well as free [14, 12] boundary conditions. In some cases one can study the existence of spiral chimeras using a self-consistency equation [14] similar to that used for spot and stripe chimera patterns in [23, 24]. However, except for the recent work [10] little is known about the stability of spiral chimeras and the more complicated solutions bifurcating from them. In order to address this problem we use here a similar setting as in [28, 29]. Employing periodic boundary conditions and a coupling kernel composed of two Fourier modes, we use the finite rank property of the corresponding convolution operator to facilitate the stability analysis. At the same time, varying the parameters of the coupling kernel generates a variety of instabilities and hence new solution types. Our stability analysis is performed in the continuum limit, using the Ott–Antonsen procedure [21, 22] in the form suggested in [9, 19]. We expect that our results will be useful for interpreting experimental data obtained in systems of coupled chemical oscillators [27, 16]. Moreover, our techniques – with some modifications – are also applicable to more complicated three-dimensional chimera patterns [13, 11].

The paper is organized as follows. First, we present the two main systems studied in our investigation, a two-dimensional system of nonlocally coupled phase oscillators and the corresponding continuum limit equation, and summarize our main results in Figure 2. In Section 2 we recall the details of the stability analysis for relative equilibria of the Ott–Antonsen equation, which we use to determine stability boundaries of symmetric four-core and 16-core spiral chimera states. In Section 3 we classify instabilities of the symmetric four-core spiral chimera and discuss properties of the new solutions found in the finite system (1) by numerical continuation. Some concluding remarks are given in Section 4.

Two Appendices at the end of the paper summarize the details of the mathematical steps that are used in our treatment of the characteristic equation for the four-core and 16-core spiral chimeras to optimize the efficiency of our numerical solvers.

1.1 Phase oscillator model

We consider a two-dimensional square lattice of nonlocally coupled phase oscillators $\{\Psi_{jk}(t)\}_{j,k=1}^N$ evolving according to

$$\frac{d\Psi_{jk}}{dt} = - \sum_{m,n=1}^N G\left(\frac{2\pi}{N}(j-m), \frac{2\pi}{N}(k-n)\right) \sin(\Psi_{jk} - \Psi_{mn} + \alpha), \quad (1)$$

where $\alpha \in (-\pi/2, \pi/2)$ is the phase lag parameter and $G : \mathbb{R}^2 \rightarrow \mathbb{R}$ is the coupling function. The function G is assumed to be 2π -periodic with respect to both arguments, a requirement that is equivalent to imposing periodic boundary conditions on the boundary of the fundamental domain. We choose, following [29], the parametrized coupling function

$$G(x, y) = \cos x + \cos y + \gamma(\cos 2x + \cos 2y), \quad \gamma \in \mathbb{R}. \quad (2)$$

This coupling function has D_4 symmetry, i.e., it is invariant under the pair of reflections $(x, y) \rightarrow (-x, y)$ and $(x, y) \rightarrow (x, -y)$, as well as reflections in the diagonal $(x, y) \rightarrow (y, x)$, and represents a generalization of the case with $\gamma = 1$ employed in [29]. In the following we explore the transitions in this system in the (α, γ) parameter space.

1.2 Ott–Antonsen equation

In the large N limit, the macroscopic dynamics of the system (1)–(2) is described by the Ott–Antonsen equation [21, 22]

$$\frac{dz}{dt} = \frac{1}{2}e^{-i\alpha}\mathcal{G}z - \frac{1}{2}e^{i\alpha}z^2\mathcal{G}\bar{z} \quad (3)$$

for the local order parameter $z(\cdot, t) \in C_{\text{per}}([-\pi, \pi]^2; \mathbb{C})$, where

$$(\mathcal{G}\varphi)(x, y) := \int_{-\pi}^{\pi} dx' \int_{-\pi}^{\pi} G(x-x', y-y')\varphi(x', y')dy' \quad (4)$$

and \bar{z} denotes the complex conjugate of z . Note that only solutions within the invariant manifold $|z(x, y)| \leq 1$ are physically meaningful solutions for the oscillator system (1)–(2) and that regions with $|z(x, y)| = 1$ correspond to coherent regions of the system.

Many complex dynamical regimes observed in the oscillator system correspond to relative equilibria of Eq. (3), given by the rotating wave Ansatz

$$z(x, y, t) = a(x, y)e^{i\Omega t} = h(|w(x, y)|^2)w(x, y)e^{i\Omega t}, \quad (5)$$

where $\Omega \in \mathbb{R}$ is the collective frequency and

$$h(s) := \begin{cases} \frac{1 - \sqrt{1-s}}{s} = \frac{1}{1 + \sqrt{1-s}} & \text{for } 0 \leq s < 1, \\ \frac{1 - i\sqrt{s-1}}{s} = \frac{1}{1 + i\sqrt{s-1}} & \text{for } s \geq 1. \end{cases} \quad (6)$$

In terms of $w(x, y)$ the boundary between coherence and incoherence is given by

$$|w(x, y)| = 1, \quad (7)$$

since according to (6) we have $|z(x, y)| = 1$ iff $|w(x, y)| \geq 1$.

One can easily verify that expression (5) does indeed determine a solution of Eq. (3) provided $w \in C_{\text{per}}([-\pi, \pi]^2; \mathbb{C})$ and that the parameters Ω and α then satisfy the self-consistency equation

$$\mu w(x, y) = \int_{-\pi}^{\pi} dx' \int_{-\pi}^{\pi} G(x - x', y - y') h(|w(x', y')|^2) w(x', y') dy', \quad (8)$$

where

$$\mu = i\Omega e^{i\alpha} = -\Omega e^{-i\beta} \quad \text{and} \quad \beta := \frac{\pi}{2} - \alpha. \quad (9)$$

1.3 Main results

As a primary state, we take the symmetric four-core spiral chimera (Figure 1, upper row). We determine the stability of this state and investigate the new patterns emerging from its stability boundaries. The state can be identified as a relative equilibrium (5) of the Ott–Antonsen equation (3), where

$$w(x, y) = w_p(x, y) := p(\cos x + i \cos y), \quad p \in (0, \infty), \quad (10)$$

and the dependence of the solution parameters p and Ω on the system parameters β and γ is determined from Eq. (8).

The linearization of Eq. (3) around this solution allows us to determine its stability region in the (β, γ) plane (Figure 2, shaded region). The boundary of this region consists of three curves, two of them Hopf bifurcation curves (solid blue curves) and the third a line of symmetry-breaking bifurcation (black dashed line). The two Hopf curves intersect at a codimension-two point corresponding to a nonresonant double Hopf bifurcation. All three curves have been determined by numerically solving the characteristic equation resulting from the linear stability problem arising from the Ott–Antonsen equation.

Other types of spiral chimeras that can be given explicitly as relative equilibria (5) are the 16-core spiral chimeras (Figure 1, lower row) with

$$w(x, y) = W_p(x, y) := p(\cos 2x + i \cos 2y), \quad p \in (0, \infty), \quad (11)$$

and the D_2 -symmetric four-core spiral chimeras (Figure 2, state (c)) with

$$w(x, y) = c_1 \cos x + c_2 \cos 2x + c_3 \cos y + c_4 \cos 2y, \quad (12)$$

where the unknown solution parameters $c_1, c_2, c_3, c_4 \in \mathbb{C}$ can again be determined from (8). Performing the stability analysis for the 16-core spiral (see also Figure 1 (lower row)) we find it to be stable in the large region above the red curve of Hopf bifurcations and to the right of the line $\beta = \beta_0$. The

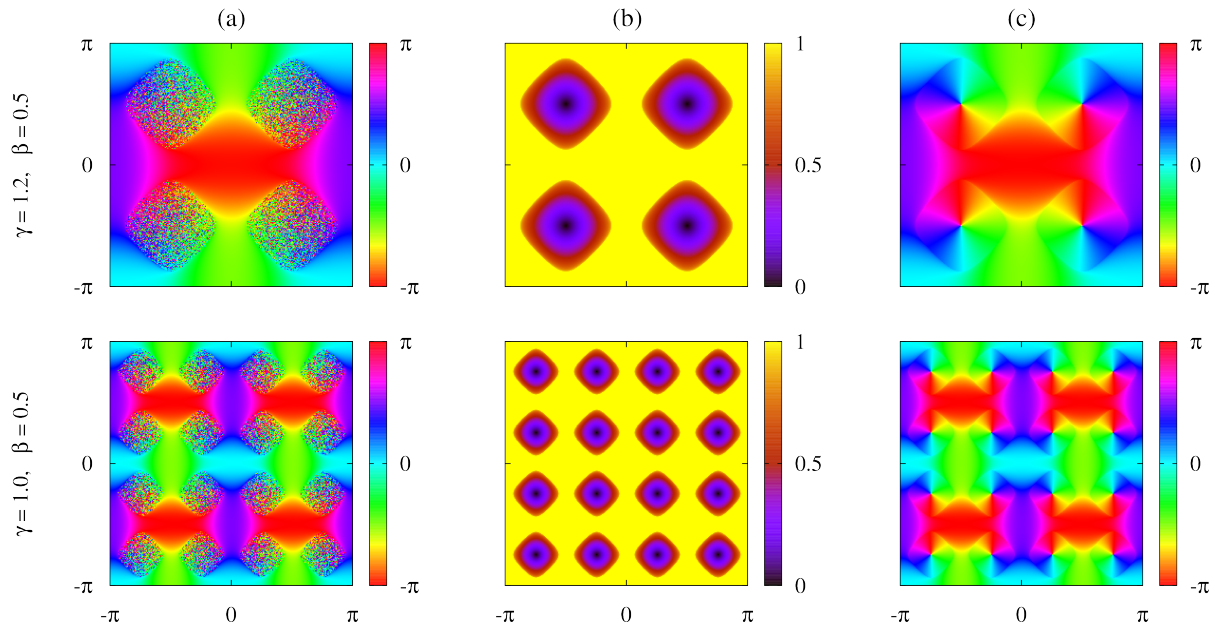


Figure 1: Four-core (upper row) and 16-core (lower row) spiral chimeras. (a) Phase snapshots in the system (1)–(2). (b) Modulus and (c) argument of the complex order parameter $a(x, y)$ of the corresponding rotating wave (5) in the Ott–Antonsen equation with $w(x, y)$ determined by (10) and (11), respectively.

D_2 -symmetric state exists only within the region bounded by the solid black curves, calculated as fold bifurcations when solving for the free parameters in (12). Numerical simulation of the system (1)–(2) shows that this state is stable only in part of this parameter region. Both these states therefore coexist stably with the primary four-core spiral chimera for appropriate choice of parameters.

The side panels in Figure 2 show several other chimera states found by numerical simulation of the system (1)–(2) at locations outside the dashed stability region of the primary spiral chimera indicated with the black crosses. Each colored symbol refers to one type of pattern and indicates the parameter values where patterns of this type have been observed. Except for state (c), these patterns can be found numerically by starting with a stable primary spiral chimera and changing parameters quasistatically so as to destabilize this state. These new spiral states turn out to have quasiperiodically evolving local order parameters and we study them mostly numerically. Figure 2 does not show states obtained by crossing the stability boundaries of the 16-core spiral. For example, when γ decreases through the red Hopf curve the 16-core spiral evolves to a plane wave suggesting that this Hopf bifurcation is subcritical. This state is not shown: in this paper we ignore all nonspiral chimera solutions such as two-stripe chimera patterns with

$$w(x, y) = p \cos x, \quad p \in (0, \infty),$$

or four-stripe chimera patterns with

$$w(x, y) = p \cos 2x, \quad p \in (0, \infty),$$

which have also been observed in the system (1)–(2) [29]. In many cases these coexist stably with the spiral chimera states we do discuss.

The symmetries of the system originate from the phase shift invariance of the form

$$z(x, y, \cdot) \rightarrow e^{i\phi} z(x, y, \cdot), \quad \phi \in S^1 \quad (13)$$

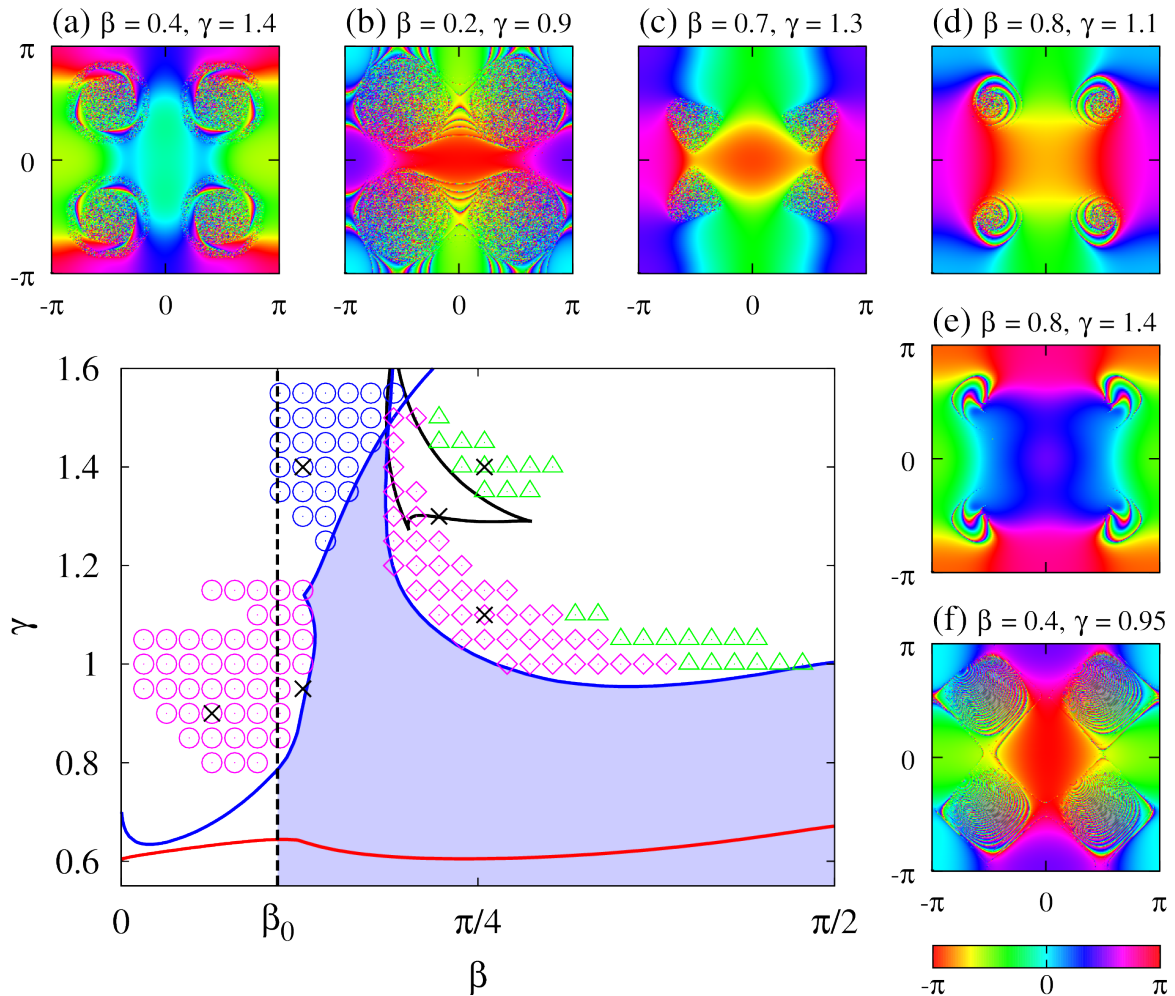


Figure 2: Stability region (blue shaded) of the four-core spiral chimeras (10) shown in Figure 1 (upper row) bounded by Hopf bifurcation curves (solid blue), and a vertical line of symmetry-breaking bifurcations ($\beta = \beta_0 \approx 0.34$, dashed black). Panels (a)–(f) show the numerically observed patterns at the parameter values given by black crosses. Patterns similar to (a) are observed at locations indicated by blue circles, with patterns similar to (b) indicated by red circles, (d) by red diamonds and (e) by green triangles. For patterns of type (c), given by (12), the existence region is bounded by the solid black curve. 16-core spiral chimeras are stable in the region above the red Hopf curve and to the right of the dashed symmetry-breaking bifurcation.

and the spatial symmetries of the fundamental domain. For the finite oscillator system (1)–(2), these are the discrete shifts, reflections and rotations by $\pi/2$ of the square lattice. In the continuum limit translations in the x and y direction are continuous symmetries as well. The phase shift symmetry has been used to define the relative equilibria in Eq. (5). Solutions that are time-periodic modulo a phase shift may possess spatio-temporal symmetries corresponding to invariance under a fixed time shift commensurate with the period, together with a discrete spatial symmetry action. Consequently the states shown in Figure 2 can be distinguished by the symmetries keeping them invariant. The symmetric four-core state shown in Figure 1 (upper row) is invariant under the following symmetry operations:

$$\begin{aligned}\kappa_1 &: z(x, y, \cdot) \rightarrow z(x, -y, \cdot) \\ \kappa_2 &: z(x, y, \cdot) \rightarrow z(-x, y, \cdot) \\ \kappa_3 &: z(x, y, \cdot) \rightarrow e^{-i\pi/2} z(\pi - y, x, \cdot).\end{aligned}$$

Note that κ_1 and κ_2 are both reflections and hence elements of order two ($\kappa_1^2 = 1, \kappa_2^2 = 1$), while κ_3 is a spatial rotation by $\pi/2$ together with a corresponding phase shift, providing a group element of order four ($\kappa_3^4 = 1$). These group actions are not independent, however, since $\kappa_2 = \kappa_3 \kappa_1 \kappa_3^{-1} \equiv \kappa_3 \kappa_1 \kappa_3^3$. Thus, the instantaneous spatial symmetries of the state are represented by the group Γ generated by the elements κ_1 and κ_3 . It turns out that Γ is a 16 element nonabelian group of generalized dihedral type. The 16-core spiral state (11) has additional symmetries given by translations by half the length of the fundamental domain in both directions. In contrast, the state (12) shown in panel (c) is invariant under κ_1 and κ_2 only and hence has D_2 -symmetry. The states in panels (a), (b), (d) are all quasiperiodic states. Specifically, they are periodic in a reference frame rotating with the collective frequency Ω , owing to the appearance of filaments of coherent oscillators that rotate with a new frequency about each incoherent core. Such rotating filaments can be seen in panel (e) albeit in a case where they rotate about a phase singularity rather than an incoherent core. In particular, the state in panel (a) possesses a spatio-temporal symmetry where a time shift by half the new period can be compensated by κ_3^2 . Finally, panel (f) shows a state with translational motion in time. Such a state can be viewed as a periodic solution modulo a lateral translation by the width of the fundamental domain.

We emphasize that the symmetries identified above are the symmetries associated with the continuum limit; in the discrete case the symmetry will necessarily be only approximate, although departures from continuous symmetry decrease as the number of oscillators increases, see [18]. We also note that if the quasiperiodic states are time-averaged the D_4 -symmetry of the system is restored *on average*, cf. [2].

2 Preliminaries

2.1 Stability

Starting from a solution $w(x, y)$ of the self-consistency equation (8), which provides a rotating wave of the form (5), we can analyze its stability by substituting

$$z(x, y, t) = (a(x, y)e^{i\beta} + v(x, y, t))e^{i\Omega t}$$

into the Ott–Antonsen equation (3) and linearizing with respect to the small perturbation $v(x, y, t)$. This procedure results in the linear but nonautonomous eigenvalue problem

$$\frac{dv}{dt} = -\Omega\eta(|w(x, y)|^2)v + \frac{1}{2}e^{-i\alpha}(\mathcal{G}v + a^2(x, y)\mathcal{G}\bar{v}), \quad (14)$$

where both $w(x, y)$ and $a(x, y)$ are given by the underlying rotating wave (5) and

$$\eta(s) = -i(h(s)s - 1) = \begin{cases} i\sqrt{1-s} & \text{for } 0 \leq s < 1, \\ -\sqrt{s-1} & \text{for } s \geq 1. \end{cases} \quad (15)$$

Equation (14) can be studied in a similar manner to that described in detail for Eq. (63) in [19]: the linear operator appearing in Eq. (14) is a sum of the multiplication operator $-\Omega\eta(|w(x, y)|^2)$ and a compact integral operator. The essential spectrum of this operator depends on the multiplication operator only and is given by the expression

$$\sigma_{\text{ess}} = \{-\Omega\eta(|w(x, y)|^2) : (x, y) \in [-\pi, \pi]^2\} \cup \{\text{c.c.}\} \subset \mathbb{R} \cup i\mathbb{R}. \quad (16)$$

Note that the operator in Eq. (14) includes complex conjugation of its argument and hence cannot be treated immediately as a complex operator. Instead, in order to obtain the point spectrum it is convenient to solve for eigenmodes of the form

$$v(x, y, t) = v_+(x, y)e^{\lambda t} + \bar{v}_-(x, y)e^{\bar{\lambda}t}. \quad (17)$$

This provides a solution to Eq. (14), if the eigenvalue λ and the components $(v_+, v_-)^T$ of the eigenmode satisfy

$$\lambda \begin{pmatrix} v_+ \\ v_- \end{pmatrix} = \begin{pmatrix} -\Omega\eta(|w|^2)v_+ + \frac{1}{2}e^{-i\alpha}(\mathcal{G}v_+ + a^2\mathcal{G}v_-) \\ -\Omega\overline{\eta(|w|^2)}v_- + \frac{1}{2}e^{i\alpha}(\mathcal{G}v_- + \bar{a}^2\mathcal{G}v_+) \end{pmatrix},$$

or equivalently

$$\begin{pmatrix} v_+ \\ v_- \end{pmatrix} = \frac{1}{2} \begin{pmatrix} e^{-i\alpha}(\lambda + \Omega\eta(|w|^2))^{-1}(\mathcal{G}v_+ + a^2\mathcal{G}v_-) \\ e^{i\alpha}(\lambda + \Omega\overline{\eta(|w|^2)})^{-1}(\mathcal{G}v_- + \bar{a}^2\mathcal{G}v_+) \end{pmatrix}. \quad (18)$$

Applying the integral operator \mathcal{G} to both sides of Eq. (18), we obtain the nonlocal eigenvalue problem

$$\begin{pmatrix} V_+ \\ V_- \end{pmatrix} = \frac{1}{2} \begin{pmatrix} e^{-i\alpha}\mathcal{G} \left[(\lambda + \Omega\eta(|w|^2))^{-1} (V_+ + a^2V_-) \right] \\ e^{i\alpha}\mathcal{G} \left[(\lambda + \Omega\overline{\eta(|w|^2)})^{-1} (V_- + \bar{a}^2V_+) \right] \end{pmatrix} \quad (19)$$

for the components

$$V_+(x, y) := (\mathcal{G}v_+)(x, y), \quad V_-(x, y) = (\mathcal{G}v_-)(x, y), \quad (20)$$

of the eigenmode of the local mean field $V := \mathcal{G}v$. Note that if (λ, V_+, V_-) is a solution of the problem (19) so is $(\bar{\lambda}, \bar{V}_-, \bar{V}_+)$. It follows that the eigenvalues λ are either real or occur in complex-conjugate pairs. Further structural properties of the solutions of (19), equivalently of (18), are the following:

Proposition 1 Suppose Eq. (3) has a solution of the form (5) with coherent and incoherent domains $D_C \cup D_I = [-\pi, \pi]^2$, such that

$$|a(x, y)| = 1 \quad \text{iff} \quad (x, y) \in D_C.$$

Moreover, suppose that $(\lambda, v_+(x, y), v_-(x, y))$ is a solution of the nonlocal eigenvalue problem (18). Then the corresponding eigenmode $v(x, y, t)$ given by (17) has the following properties:

(i) there exists a function $C : D_C \rightarrow \mathbb{R}$ such that

$$v(x, y, t) = iC(x, y, t)a(x, y)e^{i\beta}, \quad (21)$$

(ii) if $\lambda = i\omega_0$, where $\omega_0 \in \mathbb{R} \setminus \{0\}$, then for all t the eigenmode $v(x, y, t)$ is unbounded along the contour determined by the equation

$$|w(x, y)|^2 = 1 - (\omega_0/\Omega)^2. \quad (22)$$

This singularity contour lies completely in the incoherent domain D_I .

Proof: (i) From Eqs. (18) and (20) we obtain

$$\begin{aligned} v(x, y, t) = v_+(x, y)e^{\lambda t} + \bar{v}_-(x, y)e^{\bar{\lambda}t} &= \frac{1}{2}e^{-i\alpha} \left[(\lambda + \Omega\eta(|w|^2))^{-1} (V_+ + a^2V_-) e^{\lambda t} \right. \\ &\quad \left. + (\bar{\lambda} + \Omega\eta(|w|^2))^{-1} (a^2\bar{V}_+ + \bar{V}_-) e^{\bar{\lambda}t} \right]. \end{aligned} \quad (23)$$

For $(x, y) \in D_C$ we have $|a(x, y)| = 1$, and expressions (5) and (6) therefore imply that

$$a^{-1}(x, y) = \bar{a}(x, y) \quad \text{for all} \quad (x, y) \in D_C.$$

Similarly, formula (15) yields

$$\bar{\eta}(|w(x, y)|^2) = \eta(|w(x, y)|^2) \quad \text{for all} \quad (x, y) \in D_C.$$

Inserting this result into (23) we obtain

$$v(x, y, t) = e^{-i\alpha} a(x, y) \operatorname{Re} \left((\lambda + \Omega\eta(x, y))^{-1} (\bar{a}(x, y)V_+ + a(x, y)V_-) e^{\lambda t} \right),$$

which is equivalent to the claim (21).

(ii) Expression (18) shows that the functions $v_+(x, y)$ and $v_-(x, y)$ are singular for $\lambda + \Omega\eta(|w|^2) = 0$ and $\lambda + \Omega\bar{\eta}(|w|^2) = 0$, respectively. When $\lambda = i\omega_0$ their linear combination $v(x, y, t)$ is therefore singular along the curve/curves determined by the condition

$$\left| i\omega_0 + \Omega\eta(|w(x, y)|^2) \right| \left| i\omega_0 + \Omega\bar{\eta}(|w(x, y)|^2) \right| = 0.$$

Because of the definition (15), this equation has no solutions for $|w| \geq 1$, whereas for $|w| < 1$ it can be rewritten in the form

$$\omega_0^2 + \Omega^2\eta^2(|w|^2) = \omega_0^2 - \Omega^2(1 - |w|^2) = 0. \quad (24)$$

This conditions is equivalent to (22) and implies $|w|^2 < 1$, and hence incoherence. ■

Remark 1 *The geometry behind assertion (i) of Proposition 1 is as follows. Let $v(l) \in \mathbb{C}$ be a smooth function such that $|v(l)| = 1$ in the interval $l \in (l_0 - \varepsilon, l_0 + \varepsilon)$ for some $l_0, \varepsilon > 0$. This assumption is equivalent to the identity $v(l)\bar{v}(l) = 1$. Differentiating with respect to l we obtain*

$$v'(l_0)\bar{v}(l_0) + v(l_0)\bar{v}'(l_0) = 2\operatorname{Re}(v'(l_0)\bar{v}(l_0)) = 0.$$

Hence there exists a constant $c_0 \in \mathbb{R}$ such that $v'(l_0)\bar{v}(l_0) = ic_0$. Multiplying this identity by $v(l_0)$ and taking into account that $|v(l_0)| = 1$ we obtain

$$v'(l_0) = ic_0v(l_0). \quad (25)$$

Now, interpreting the complex numbers $v(l)$ as planar vectors we see that the necessary condition for $|v(l)| = 1$ in the vicinity of $l = l_0$ is that the tangent vector $v'(l_0)$ is perpendicular to the vector $v(l_0)$.

2.2 Finite-rank operator

Solving the integral equations for the chimera states and their stability properties typically requires substantial computational effort. However, reformulating the equations in terms of the local mean fields leads to significant reduction in computational complexity whenever the coupling kernel (2) is such that the corresponding convolution operator \mathcal{G} is of finite rank. In this case, one can search for the unknown profile of both the chimera state and its perturbation within a finite-dimensional space. This approach has been elaborated for the self-consistency equation determining the chimera profiles in [1] and was extended to the stability problem in [19]. For the two-dimensional problem with the kernel function used here, this method was used already in [28, 29]. Here, it means that we can solve for the perturbations $V = (V_+, V_-)^T$ of the local mean field as linear combinations

$$V = \begin{pmatrix} V_+ \\ V_- \end{pmatrix} = \sum_{k=1}^8 \hat{V}_k \psi_k(x, y), \quad (26)$$

of eight basis functions

$$(\psi_1(x, y), \dots, \psi_8(x, y))^T = (\cos x, \cos y, \cos 2x, \cos 2y, \sin x, \sin y, \sin 2x, \sin 2y)^T \quad (27)$$

spanning the range of \mathcal{G} . Collecting the eight pairs of complex coefficients $\hat{V}_k \in \mathbb{C}^2$, $k = 1, \dots, 8$, into a single vector $\hat{V} \in \mathbb{C}^{16}$, we can rewrite Eq. (19) as an equivalent matrix equation

$$\hat{V} = \frac{1}{2}B(\lambda)\hat{V}, \quad (28)$$

where we solve for the eigenvalue λ and the corresponding kernel vector $\hat{V} \in \mathbb{C}^{16}$. The matrix $B(\lambda)$ consists of 2×2 blocks:

$$B_{mn}(\lambda) = \begin{pmatrix} e^{-i\alpha} \left\langle (\lambda + \Omega\eta(|w|^2))^{-1} \psi_m \psi_n \right\rangle & e^{-i\alpha} \left\langle (\lambda + \Omega\eta(|w|^2))^{-1} a^2 \psi_m \psi_n \right\rangle \\ e^{i\alpha} \left\langle (\lambda + \Omega\bar{\eta}(|w|^2))^{-1} \bar{a}^2 \psi_m \psi_n \right\rangle & e^{i\alpha} \left\langle (\lambda + \Omega\bar{\eta}(|w|^2))^{-1} \psi_m \psi_n \right\rangle \end{pmatrix}$$

for first harmonic components, $m = 1, 2, 5, 6$, and

$$B_{mn}(\lambda) = \begin{pmatrix} \gamma e^{-i\alpha} \left\langle (\lambda + \Omega\eta(|w|^2))^{-1} \psi_m \psi_n \right\rangle & \gamma e^{-i\alpha} \left\langle (\lambda + \Omega\eta(|w|^2))^{-1} a^2 \psi_m \psi_n \right\rangle \\ \gamma e^{i\alpha} \left\langle (\lambda + \Omega\bar{\eta}(|w|^2))^{-1} \bar{a}^2 \psi_m \psi_n \right\rangle & \gamma e^{i\alpha} \left\langle (\lambda + \Omega\bar{\eta}(|w|^2))^{-1} \psi_m \psi_n \right\rangle \end{pmatrix}$$

for second harmonic components, $m = 3, 4, 7, 8$. Here the angled brackets $\langle \cdot \rangle$ denote the integral

$$\langle \varphi \rangle := \int_{-\pi}^{\pi} dx \int_{-\pi}^{\pi} \varphi(x, y) dy,$$

where $\varphi \in C([-\pi, \pi]^2; \mathbb{C})$ is an arbitrary function. The eigenvalues λ can be found as solutions of the characteristic equation

$$\det \left[I_{16} - \frac{1}{2} B(\lambda) \right] = 0,$$

where I_n denotes the $n \times n$ identity matrix. Having solved in this way for the eigenvalue λ the kernel vector $(\hat{V}_1, \dots, \hat{V}_8) \in \mathbb{C}^{16}$ can be transformed into the components of the corresponding eigenmode $(v_+(x, y), v_-(x, y))$ using the formulas (18), (20) and (26).

Note that according to (16) the incoherent core always generates an essential spectrum on the imaginary axis. Hence, critical eigenvalues can interact with the essential spectrum and classical center-manifold theory is not applicable. This fact is related to the fact that eigenmodes become singular when the corresponding eigenvalue approaches the imaginary axis. Despite this complication we refer in the following to the associated bifurcations according to their critical point spectrum, e.g. as Hopf bifurcations.

3 Results

3.1 Symmetric four-core spiral chimera

Recall that for a symmetric four-core spiral chimera the local mean field w_p , given by expression (10), the inequalities $|w_p(x, y)| \geq 1$ and $|w_p(x, y)| < 1$ identify the coherent and incoherent regions D_C and D_I , respectively. These regions are both nonempty for $p > 1/\sqrt{2}$ only and the coherence-incoherence boundary is then determined by the equation

$$\cos^2 x + \cos^2 y = p^{-2}. \quad (29)$$

The discrete symmetries of such a pattern, which we discussed in Section 1.3, leads to a block-diagonal structure of the matrix $B(\lambda)$:

$$B(\lambda) = \begin{pmatrix} B_{11}(\lambda) & B_{12}(\lambda) & 0 & 0 & 0 & 0 & 0 & 0 \\ B_{21}(\lambda) & B_{22}(\lambda) & 0 & 0 & 0 & 0 & 0 & 0 \\ 0 & 0 & B_{33}(\lambda) & B_{34}(\lambda) & 0 & 0 & 0 & 0 \\ 0 & 0 & B_{43}(\lambda) & B_{44}(\lambda) & 0 & 0 & 0 & 0 \\ 0 & 0 & 0 & 0 & B_{55}(\lambda) & 0 & 0 & 0 \\ 0 & 0 & 0 & 0 & 0 & B_{66}(\lambda) & 0 & 0 \\ 0 & 0 & 0 & 0 & 0 & 0 & B_{77}(\lambda) & 0 \\ 0 & 0 & 0 & 0 & 0 & 0 & 0 & B_{88}(\lambda) \end{pmatrix}.$$

This allows us to factorize the eigenvalue problem (28) into six independent subsystems. We checked carefully the characteristic equations for all these subsystems and found that only three of them can lead to unstable eigenvalues. Among these are the two subsystems given by the blocks $B_{55}(\lambda)$

and $B_{66}(\lambda)$ corresponding to symmetry related eigenvectors $V = \hat{V}_5 \sin x$ and $V = \hat{V}_6 \sin y$, respectively. Their characteristic equations coincide and take the form

$$\det \left(I_2 - \frac{1}{2} B_{55}(\lambda) \right) \equiv \det \left(I_2 - \frac{1}{2} B_{66}(\lambda) \right) = 0. \quad (30)$$

Since these equations arise from the first harmonic components in (27), the associated eigenvalues are independent of the parameter γ governing the contribution of the second harmonics. The other subsystem providing unstable eigenvalues has the form

$$\begin{pmatrix} \hat{V}_3 \\ \hat{V}_4 \end{pmatrix} = \frac{1}{2} \begin{pmatrix} B_{33}(\lambda) & B_{34}(\lambda) \\ B_{43}(\lambda) & B_{44}(\lambda) \end{pmatrix} \begin{pmatrix} \hat{V}_3 \\ \hat{V}_4 \end{pmatrix}$$

with the characteristic equation

$$\det \left[I_4 - \frac{1}{2} \begin{pmatrix} B_{33}(\lambda) & B_{34}(\lambda) \\ B_{43}(\lambda) & B_{44}(\lambda) \end{pmatrix} \right] = 0. \quad (31)$$

The corresponding eigenvectors can be found from the expression

$$V = \hat{V}_3 \cos 2x + \hat{V}_4 \cos 2y, \quad (32)$$

where $(\hat{V}_3, \hat{V}_4)^T \in \mathbb{C}^4$ is the eigenvector corresponding to Eq. (31).

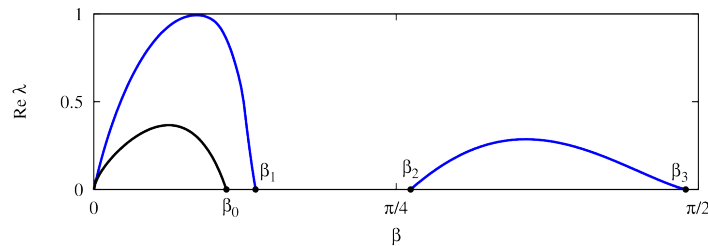


Figure 3: Unstable real eigenvalue determined by Eq. (30) (black curve) and the real part of the unstable eigenvalues determined by Eq. (31) (blue curve) for $\gamma = 1$. Bifurcation points: $\beta_0 \approx 0.34$, $\beta_1 \approx 0.42$, $\beta_2 \approx 0.82$ and $\beta_3 \approx 1.54$.

For our numerical treatment of the characteristic equations, we employed elliptic integrals to simplify the double integrals. The details of this procedure are given in the Appendices A and B. For Eq. (30), the resulting numerics show that in the interval $\beta \in (0, \beta_0)$, where $\beta_0 \approx 0.34$, there is an unstable double real root, given by the black curve in Figure 3. This root corresponds to a parity-breaking bifurcation.

In contrast to the eigenvalue from Eq. (30), eigenvalues determined by Eq. (31) depend on γ . For example, for $\gamma = 1$, Eq. (31) determines a pair of complex conjugate eigenvalues of double multiplicity that are unstable in two disjoint intervals $\beta \in (0, \beta_1) \cup (\beta_2, \beta_3)$ (blue curves in Figure 3) where $\beta_1 \approx 0.42$, $\beta_2 \approx 0.82$ and $\beta_3 \approx 1.54$ correspond to Hopf bifurcation points. Varying the parameter γ we obtain the two Hopf curves shown in blue in Figure 2. These Hopf bifurcations are responsible for the instability of the spiral chimeras at larger values of γ , whereas for smaller γ the chimeras lose stability in a steady state symmetry-breaking bifurcation as β decreases below β_0 . This bifurcation leads to chimera states that drift, i.e., the bifurcation along the line $\beta = \beta_0$ is a parity-breaking bifurcation. Note that owing to the symmetry-induced degeneracy this bifurcation produces a pair of

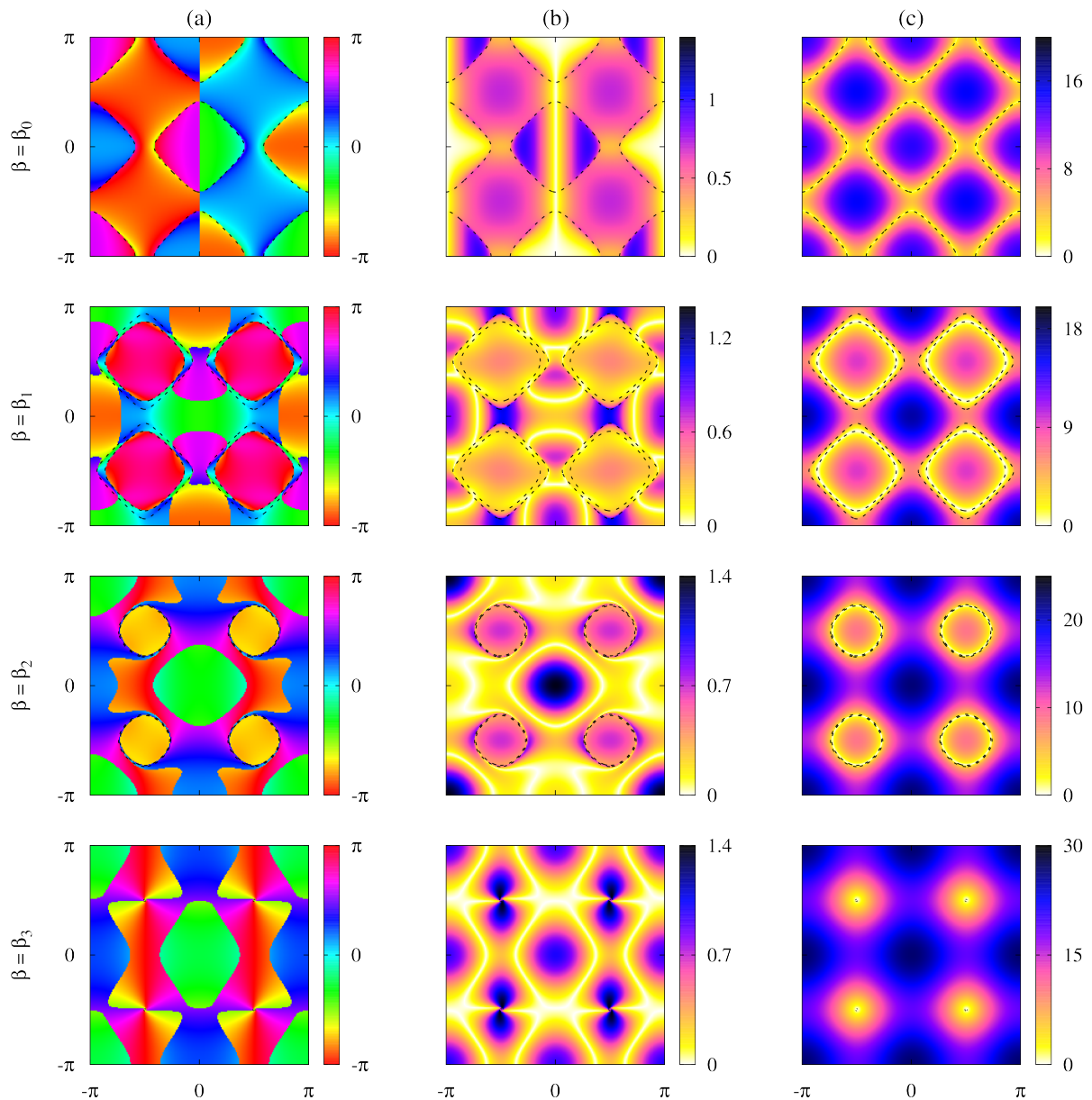


Figure 4: Marginal eigenmodes $v(x, y, 0)$ determined by expression (17) for the symmetric four-core spiral chimera pattern at the four bifurcation points $\beta = \beta_0, \beta_1, \beta_2, \beta_3$ when $\gamma = 1$. Columns (a), (b) and (c) show $\arg v(x, y)$, $|(\lambda_{\text{cr}} + \Omega(|w(x, y)|^2))v(x, y)|$ and $|\lambda_{\text{cr}} + \Omega(|w(x, y)|^2)|$, respectively, where λ_{cr} denotes the critical eigenvalue at the corresponding bifurcation point. Dashed lines show the position of the coherence-incoherence boundary and of the singularity contour (for $\beta = \beta_3$ these lines are hardly visible because of their small size).

solution branches, one consisting of solutions that drift in the x direction and the other with symmetry-related solutions that drift in the y direction. However, in the present case both drifting states are unstable and the system evolves to another state.

In Figure 4 we show the eigenmodes corresponding to the four critical eigenvalues from Figure 3. Proposition 1(ii) implies that the eigenmodes (17) corresponding to a critical eigenvalue $\lambda = i\omega_{\text{cr}}$ has a singularity along the line

$$\cos^2 x + \cos^2 y = p^{-2} \left(1 - (\omega_{\text{cr}}/\Omega_p)^2\right). \quad (33)$$

However, the corresponding quantities V_+ , V_- remain well-defined.

3.2 Quasiperiodic spiral wave chimeras

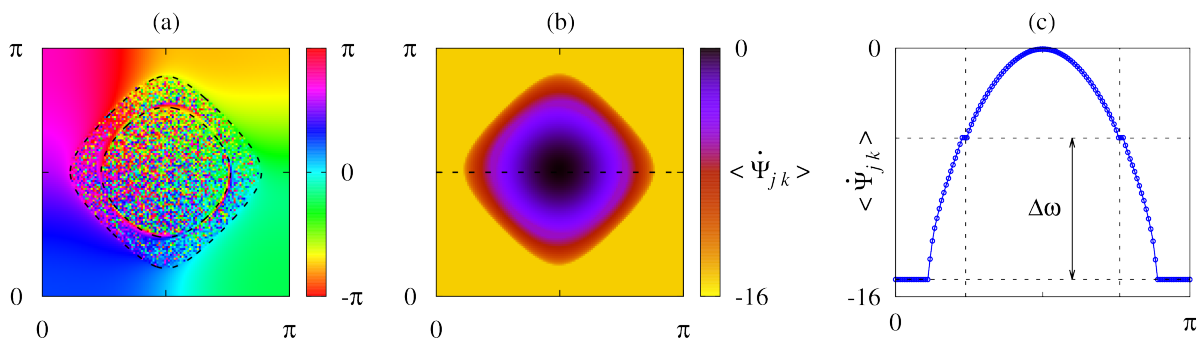


Figure 5: (a) Snapshot of the top-right core of the symmetric four-core spiral chimera pattern to the left of the left Hopf bifurcation. (b) Mean phase velocities and (c) a one-dimensional section corresponding to the dashed line in panel (b). Parameters: $N = 256$, $\gamma = 1.3$ and $\beta = 0.475$. The two dashed curves in panel (b) show the coherence-incoherence boundary (29) and the singularity curve (33) for $\beta = 0.483$, the value of β corresponding to the left Hopf bifurcation when $\gamma = 1.3$. Vertical dashed lines in panel (c) denote position of the singularity curve for $\beta = 0.483$.

Beyond the Hopf stability boundaries of the symmetric four-core spiral chimera (see Figure 2) we expect solutions of the Ott–Antonsen equation (3) that are quasiperiodic, i.e. relative periodic orbits with respect to the phase shift symmetry (13). However, as we mentioned above, due to the presence of continuous spectrum on the imaginary axis we cannot get results from classical center manifold theory about the leading order expansion of the bifurcating branch. But we can obtain some insight from the critical Hopf frequency ω_{cr} and the singular contour of the eigenmode.

Emergence of quasiperiodic spiral wave chimeras at Hopf bifurcations: In Figure 5(a) we show a quasiperiodic spiral wave chimera of the oscillator system (1) directly after a supercritical Hopf bifurcation. It turns out that this solution is characterized by a secondary region of coherence located in a narrow annular neighborhood of the singular contour of the eigenmode. Indeed, along with the large plateau corresponding to the primary region of coherence at frequency Ω the averaged frequencies in panels (b) and (c) show a small plateau located around the singular contour with a frequency close to $\Omega + \omega_{\text{cr}}$. Note that according to Proposition 1 the secondary region of coherence has to be located inside the incoherent region of the pattern on the primary branch and for the symmetric four-core spiral chimera this region has the shape of a circular annulus centered on the singularity contour (33) around the phase defect inside each incoherent core. We expect that the corresponding solutions of

the Ott–Antonsen equation (3) are relative periodic orbits with respect to the phase shift symmetry (13) and have the form

$$z(x, t) = b(x, t)e^{i\Omega t},$$

where $b(x, t)$ is periodic in t with period $2\pi/\omega$, where the new frequency $\omega \approx \omega_{\text{cr}}$. This frequency differs from Ω .

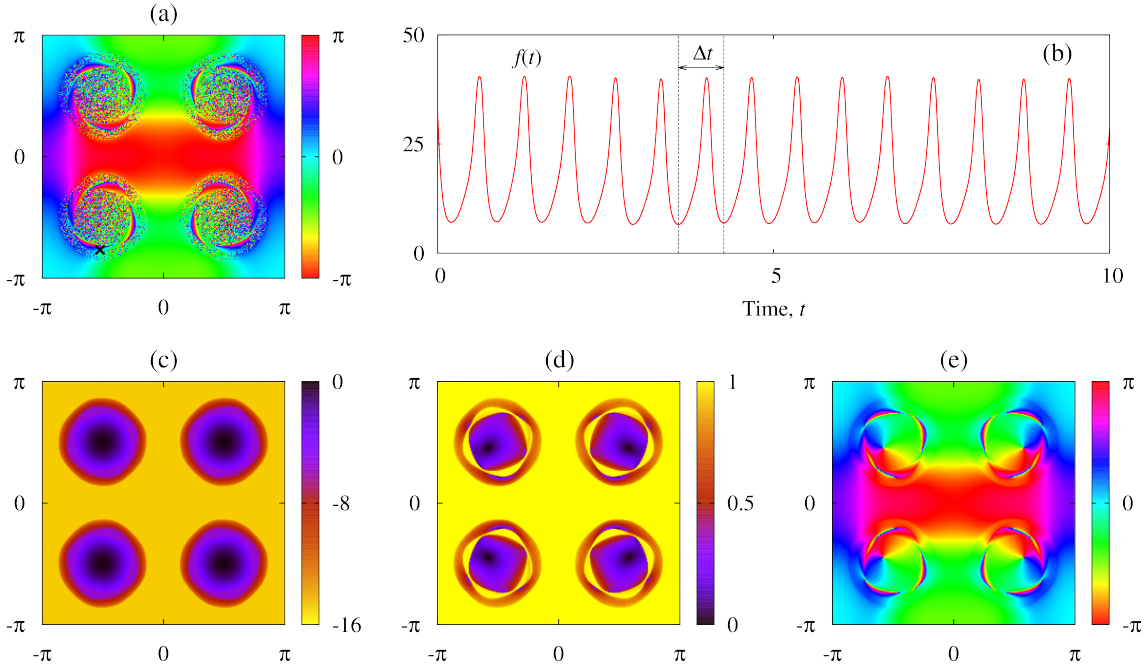


Figure 6: (a) Snapshot of a quasiperiodic spiral chimera in the system (1)–(2) for $N = 256$, $\gamma = 1.4$ and $\beta = 0.45$. (b) Indicator function $f(t)$ for $(m, n) = (61, 30)$ (cross in panel(a)) as defined in (34), showing periodic modulation with new period Δt , where Δt is the time interval between consecutive minima. (c) Mean phase velocities. (d) Modulus and (e) argument of the local order parameter Z_{jk} evaluated from expression (35).

Poincaré section: In order to study the solutions along the branch that bifurcates from the Hopf bifurcation at these values of γ we solve the oscillator system (1)–(2) numerically. The system exhibits extensive chaos in the incoherent core regions, modulated by the new frequency ω . To extract this frequency from the numerics we choose an arbitrary oscillator inside the secondary region of coherence and compare its phase $\Psi_{mn}(t)$ to the phase of the neighboring oscillator, which we also assume to be located inside the secondary region of coherence. In this way, the quantity

$$f(t) \equiv (2\pi/N)^{-1} \sin(\Psi_{mn}(t) - \Psi_{m, n-1}(t)) \quad (34)$$

isolates the new oscillation period that sets in at the Hopf bifurcation. Figure 6(b) shows that $f(t)$ has nearly periodic behavior. We therefore average the intervals Δt between successive local minima over many periods, and use the resulting average, Δt_{av} , to obtain the secondary frequency of the profile $b(x, t)$ via

$$\omega = 2\pi/\Delta t_{\text{av}}.$$

The successive minima can also be used to construct a Poincaré section and to obtain the profile $b(x, t)$ itself by calculating its average over sufficiently many snapshots taken at the crossings. In order to filter out the primary oscillation with the collective frequency Ω we have to employ phase differences between an oscillator in the core and an oscillator from the primary coherent region with

phase Ψ_{coh} . Denoting by S the set of instants at which $f(t)$ attains a local minimum we define the following expression for the local mean field at the grid points:

$$Z_{jk} = \frac{1}{|S|} \sum_{t_l \in S} e^{i(\Psi_{jk}(t_l) - \Psi_{\text{coh}}(t_l))}, \quad (35)$$

where $|S|$ is the number of elements in S . In Figs. 6(d,e) we show the modulus and argument of Z_{jk} , representing the modulus and argument of the amplitude $b(x, t)$, respectively. We see that $|b(x, t)| = 1$ in both the primary and the secondary frequency synchronized regions, indicating coherence as supposed. On the other hand, if we compute the difference $\Delta\omega = \omega - \Omega$ in the quasiperiodic chimera state and plot it as a function of β , we find that as $\beta \rightarrow \beta_{\text{cr}}$ this difference tends to ω_{cr} (see Figure 7).

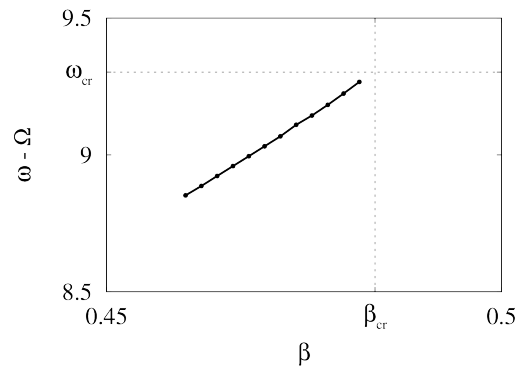


Figure 7: Difference between the secondary frequency ω and the collective frequency Ω measured for different values β . Parameters: $N = 256$ and $\gamma = 1.3$.

Numerical examples: Outside of the stability region of the symmetric four-core spiral chimera (shaded in Figure 2) we performed a numerical study of the oscillator system (1)–(2). In a dynamical continuation procedure we varied the parameter β for various fixed choices of γ and recorded the value of the classical Kuramoto order parameter

$$r(t) = \left| \frac{1}{N^2} \sum_{m,n=1}^N e^{i\Psi_{mn}(t)} \right|.$$

Whereas for the basic symmetric four-core spiral chimeras this parameter stays close to zero (blue shaded regions), it turns out to stay away from zero for most of the new states observed beyond the Hopf stability boundaries. In Figure 8 we show the behavior of $r(t)$ for β (a) decreasing through the left Hopf curve and (b) increasing through the right Hopf curve.

The transition across the left Hopf boundary corresponds to a transition from a simple spiral wave chimera, Figure 1(upper row), to a quasiperiodic spiral state similar to that shown in Figure 2(a). For larger values of γ this transition is supercritical as seen by the continuous behavior of the order parameter in Figure 8(a) but changes into an abrupt transition for smaller values of γ (Figure 8(c)). In particular, below the kink in the left Hopf bifurcation curve in Figure 2 located at $(\beta, \gamma) \approx (0.40, 1.14)$ we reach a quasiperiodic spiral chimera with a different shape (Figure 2(b)). Instead of a coherent region appearing in the incoherent core, the original coherent region breaks into several parts with several equidistant frequencies, Figure 9.

Drifting state: We also have identified a small region in parameter space with a drifting symmetry-broken state. Figure 2(f) and file beta0_4gamma0_95.avi show a snapshot and a movie of such a

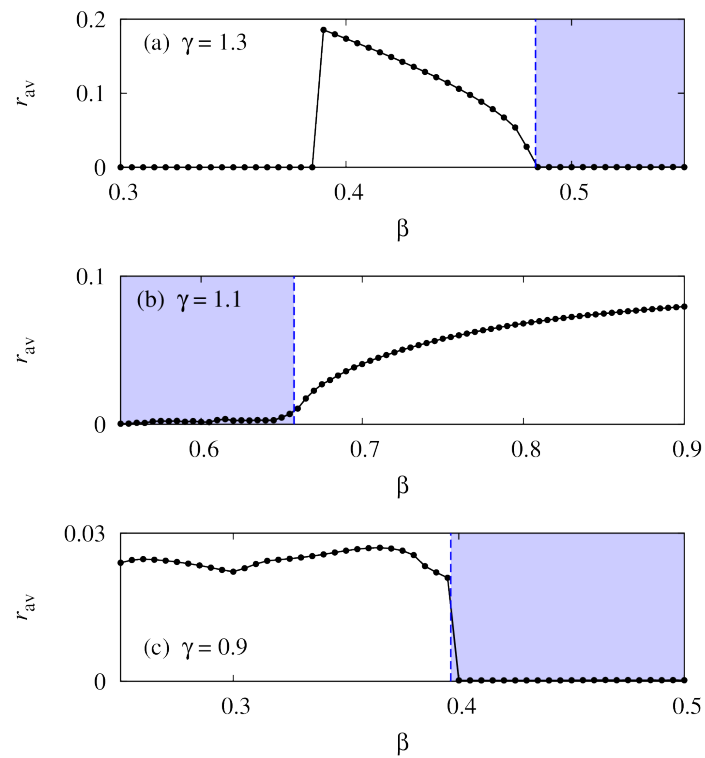


Figure 8: Time-averaged Kuramoto order parameter r_{av} (dots) for spatio-temporal patterns in system (1)–(2) with $N = 1024$. (a) $\gamma = 1.3$ and β decreasing from 0.55 to 0.3, (b) $\gamma = 1.1$ and β increasing from 0.55 to 0.9, (c) $\gamma = 0.9$ and β decreasing from 0.5 to 0.25. The dashed vertical lines show the position of the theoretically predicted Hopf bifurcations. In (a) the abrupt jump near $\beta = 0.38$ corresponds to a transition to a coherent twisted state.

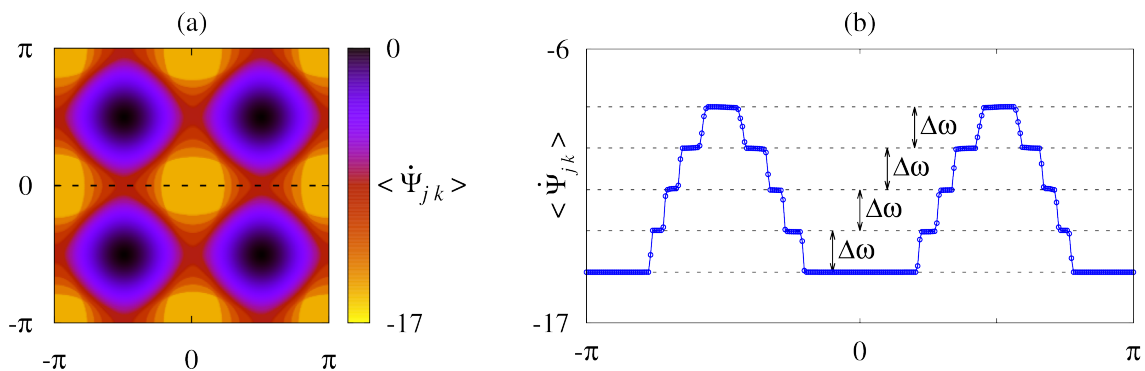


Figure 9: (a) Mean phase velocities $\langle \dot{\Psi}_{jk} \rangle$ averaged over 200 time units for the spiral chimera state shown in Figure 2(b). (b) Cross-section of the same plot along the dashed line from panel (a).

drifting state: the state is a four-core state in which the cores are no longer incoherent but instead consist of coherent oscillators. These cores exhibit subtle but unambiguous differences resulting in the breaking of the Γ -symmetry of the state. This is most easily seen in the contours connecting the two cores on the left and those on the right. There is also an asymmetry between the two top cores and the two bottom cores. Consequently both κ_1 and κ_2 symmetries are broken, and as a result the state drifts simultaneously in both x and y directions. Typically the magnitude of the nonsymmetric part of the profile fluctuates in time leading to drift whose speed and direction also fluctuate in time. As in other problems of this type these drifts are a consequence of the nonzero projection of the solution profile on the Goldstone mode present due to the translation invariance of the system. In one spatial dimension the speed of such a drifting coherent state can be found from a nonlocal nonlinear eigenvalue problem [28] but this procedure does not apply when the drift changes direction in response to time-dependent asymmetry. A detailed study of this interesting state will be undertaken in a future publication.

Genesis of filamented structures: For $\gamma \geq 1$ Figure 8(b) indicates that the Hopf bifurcation along the right stability boundary in Figure 2 is also supercritical. However, the resulting quasiperiodic spiral chimera undergoes a sequence of further transformations which we call a 'synchronization cascade'. This notion is explained in Figure 10 for $\gamma = 1.1$.

The original spiral wave chimera, Figure 1 (upper row), has four symmetrically located incoherent cores with no internal structure. For $\beta = 0.65$, i.e., just outside the right stability boundary, there is a thin ring of coherent (phase-locked) oscillators that appears in the incoherent core along the singular contour (33) whose common frequency ω differs from the frequency Ω of the coherent oscillators outside of the incoherent cores. For increasing β the coherent ring widens, while the outer incoherent ring separating the new coherent ring from the coherent spiral state outside it gradually narrows and for $\beta \geq 0.70$ disappears altogether (Figure 10, top row). The figure shows that although the two coherent regions now meet they nevertheless remain distinct. This is because the oscillators in the two coherent regions continue to rotate with different effective frequencies, a fact that manifests itself as a rotating filament outside of the remaining incoherent core. In fact, for $\beta = 0.70$ another coherent ring has already appeared in the remaining incoherent core and is beginning to grow. For increasing β this ring gives rise to a second rotating filament. A similar scenario repeats for $\beta = 0.75$ and again for $\beta = 0.80$. Thus, for $\beta = 0.90$ (Figure 10, last row) we have a four-core spiral wave chimera whose incoherent cores are surrounded by *four* rotating filaments. During this process the incoherent core decreases in size and for sufficiently large β it disappears altogether, leaving a purely coherent filamented structure (Figure 2, red triangles and panel (e)). For reasons we do not understand this sequence of events does not take place to the left of the left stability boundary.

Additional information about the localization of the filaments is obtained when we calculate and plot the phase velocity $\langle \dot{\Psi}_{jk} \rangle$ of the oscillators. The graph corresponding to the middle row of Figure 10 is shown in Figure 11. It contains three circular regions with nearly constant mean velocities and a central region where mean phase velocities vary smoothly. This behavior appears to be the consequence of the presence of three filaments that originate from the defects on the boundary of the incoherent core (the innermost black curve). Each filament in turn terminates at a defect that rotates around the incoherent core along one of the three outer black curves.

The coherent rings corresponding to different filaments are phase-locked to each other so that the resulting solution contains only a single new frequency. This frequency is localized in a bounded region inside the original incoherent core. However, because different filaments terminate at different distances from the center of the spiral there will always be radius intervals containing only one rotating filament, two such filaments etc. As a result, averaging the state in time leads to a discontinuous order parameter, albeit with D_4 -symmetry, as found in [29].

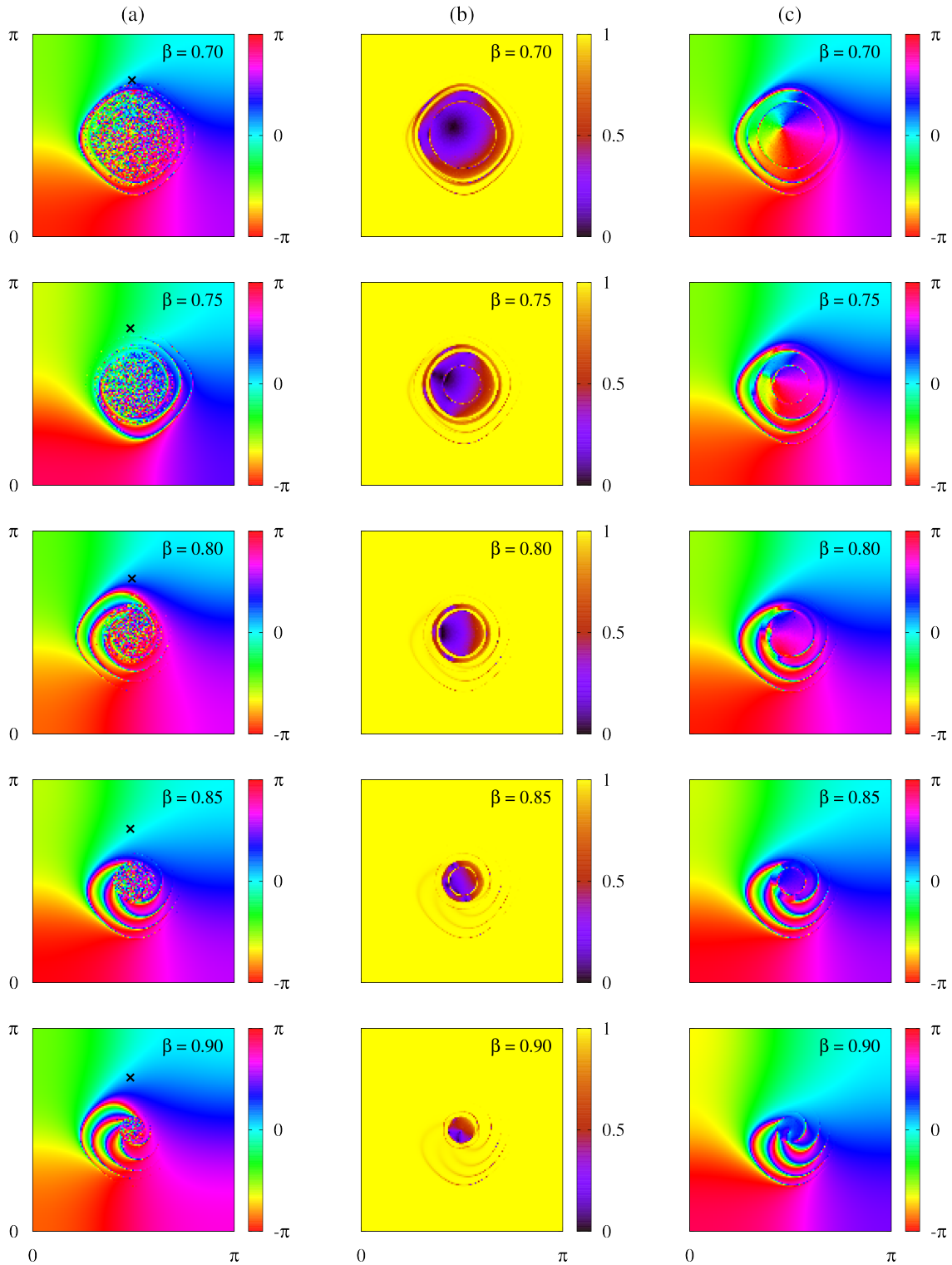


Figure 10: (a) Phase snapshots of quasiperiodic chimeras and the corresponding local order parameters: (b) modulus $|z(x, t)|$ and (c) argument $\arg z(x, t)$. Parameters $N = 256$, $\gamma = 1.1$. The black cross in each of the left panels indicates the oscillator index (n, m) used in the definition of the corresponding indicator function $f(t)$, similar to Figure 6(a).

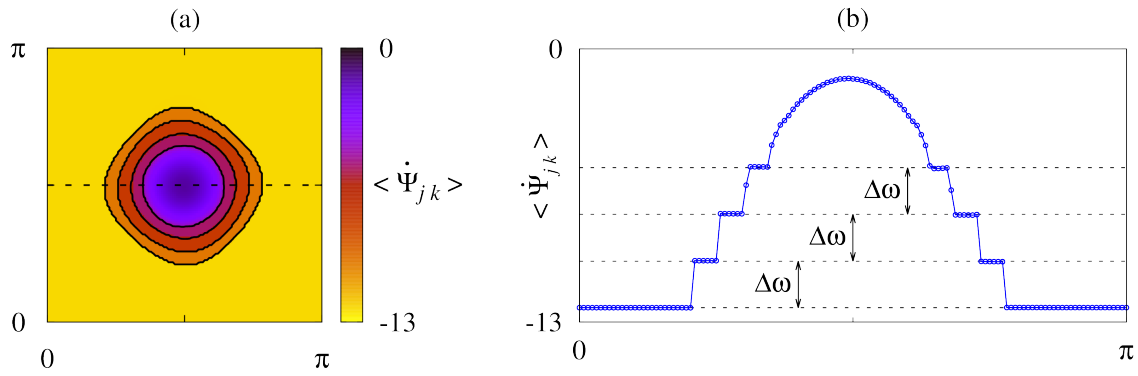


Figure 11: (a) Mean phase velocities $\langle \dot{\Psi}_{jk} \rangle$ averaged over 200 time units for the spiral chimera state shown in the third row of Figure 10. (b) Cross-section of the same plot along the dashed line from panel (a).

3.3 D_2 -symmetric four-core spiral chimera

In Figure 2(c) we show a D_2 -symmetric four-core spiral chimera state with local mean field of the form (12). From the self-consistency equation (8), we obtain for the coefficients c_j the system

$$\begin{aligned} \mu c_1 &= \int_{-\pi}^{\pi} dx \int_{-\pi}^{\pi} h(|w(x,y)|^2) w(x,y) \cos x dy, \\ \mu c_2 &= \gamma \int_{-\pi}^{\pi} dx \int_{-\pi}^{\pi} h(|w(x,y)|^2) w(x,y) \cos 2x dy, \\ \mu c_3 &= \int_{-\pi}^{\pi} dx \int_{-\pi}^{\pi} h(|w(x,y)|^2) w(x,y) \cos y dy, \\ \mu c_4 &= \gamma \int_{-\pi}^{\pi} dx \int_{-\pi}^{\pi} h(|w(x,y)|^2) w(x,y) \cos 2y dy, \end{aligned}$$

with $w(x,y)$ given by (12). Solving this system numerically when $\gamma = 1.4$, we obtain the isola shown in Figure 12. Stable solutions are found along the lower branch between the two folds at either end. Varying γ , we obtain the existence region for this solution type enclosed by the fold curves shown in black in Figure 2. For the stability analysis one can establish a matrix problem as in Section 3.1, but with a different block structure due to the different symmetry properties of the D_2 -symmetric four-core spiral chimera. However, the reduction of the double integrals by elliptic integration as elaborated in the Appendix A for the fully symmetric four-core spiral chimera does not apply here. By this reason, we did not undertake an explicit calculation of Hopf bifurcations of this state which numerical simulations suggest are present. These restrict the stability region of this state to $\gamma \leq 1.35$.

3.4 16-core spiral chimera

The 16-core spiral chimera is also determined from the corresponding self-consistency equation. To compute this type of solution we substitute the Ansatz (11) into Eq. (8) and project the resulting identity onto the $\cos 2x$ direction. We obtain

$$\mu = \frac{\gamma}{p} \int_{-\pi}^{\pi} dy \int_{-\pi}^{\pi} h(|W_p(x,y)|^2) W_p(x,y) \cos 2x dx. \quad (36)$$

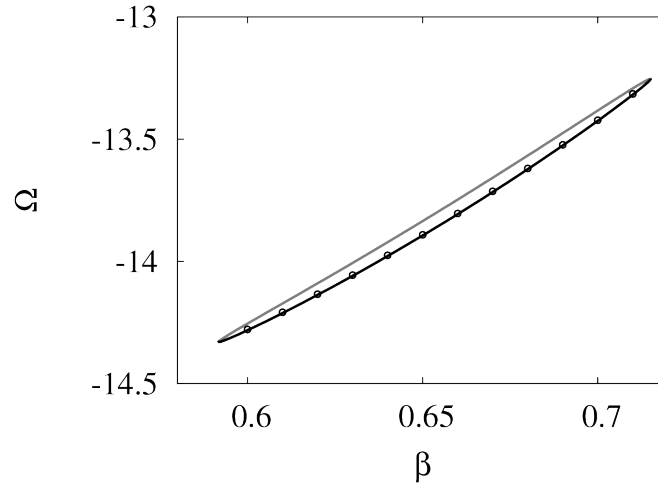


Figure 12: Stable (black) and unstable (gray) parts of an isola of D_2 -symmetric solutions of the self-consistency equation (8) corresponding to the D_2 -symmetric pattern in Figure 2(c). Circles show numerical data obtained by dynamical continuation of solutions of the system (1)–(2). Parameter: $\gamma = 1.4$.

This expression determines the pair of parameters (β, Ω) for every $\gamma > 0$, $p > 0$ and hence the rotating wave (5) with $w(x, y)$ given by (11). For $p > 1/\sqrt{2}$ this rotating wave corresponds to a coherence-incoherence pattern with the coherence-incoherence boundary determined by equation

$$\cos^2 2x + \cos^2 2y = p^{-2}.$$

Employing the symmetries of W_p we find that the matrix $B(\lambda)$ has block-diagonal structure,

$$B(\lambda) = \begin{pmatrix} B_{11}(\lambda) & 0 & 0 & 0 & 0 & 0 & 0 & 0 \\ 0 & B_{22}(\lambda) & 0 & 0 & 0 & 0 & 0 & 0 \\ 0 & 0 & B_{33}(\lambda) & B_{34}(\lambda) & 0 & 0 & 0 & 0 \\ 0 & 0 & B_{43}(\lambda) & B_{44}(\lambda) & 0 & 0 & 0 & 0 \\ 0 & 0 & 0 & 0 & B_{55}(\lambda) & 0 & 0 & 0 \\ 0 & 0 & 0 & 0 & 0 & B_{66}(\lambda) & 0 & 0 \\ 0 & 0 & 0 & 0 & 0 & 0 & B_{77}(\lambda) & 0 \\ 0 & 0 & 0 & 0 & 0 & 0 & 0 & B_{88}(\lambda) \end{pmatrix}$$

and use this fact to factorize the eigenvalue problem (28) into seven independent subsystems. Four of these generate unstable eigenvalues.

The subsystems corresponding to blocks $B_{11}(\lambda)$ and $B_{22}(\lambda)$ are identical. Their characteristic equations read

$$\det \left(I_2 - \frac{1}{2} B_{11}(\lambda) \right) \equiv \det \left(I_2 - \frac{1}{2} B_{22}(\lambda) \right) = 0. \quad (37)$$

These conditions determine a pair of complex-conjugate eigenvalues of double multiplicity which lie apart from the corresponding essential spectrum. Figure 13 shows that these eigenvalues are responsible for two intervals of instability, $\beta_4 < \beta < \beta_5$ and $\beta_6 < \beta < \pi/2$, bounded by three Hopf

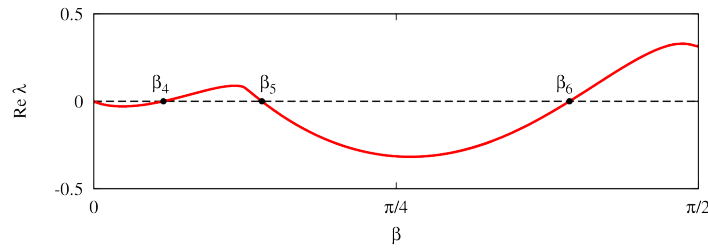


Figure 13: Real part of the eigenvalues determined by Eq. (37) for $\gamma = 0.63$. Hopf bifurcation points: $\beta_4 \approx 0.18$, $\beta_5 \approx 0.44$ and $\beta_6 \approx 1.24$.

bifurcations, at $\beta = \beta_4, \beta_5$ and β_6 . Because the multiplicity of the eigenvalues at the Hopf bifurcation is doubled, one expects oscillations aligned with either the x or the y axes, or along the diagonals.

Two other subsystems with unstable eigenvalues are those corresponding to blocks $B_{77}(\lambda)$ and $B_{88}(\lambda)$. The characteristic equations are

$$\det \left(I_2 - \frac{1}{2} B_{77}(\lambda) \right) \equiv \det \left(I_2 - \frac{1}{2} B_{88}(\lambda) \right) = 0. \quad (38)$$

By a simple rescaling argument one can show that the block $B_{77}(\lambda)$ of a 16-core spiral chimera with $w(x, y) = W_p(x, y)$ is equal to the matrix block $B_{55}(\lambda/\gamma)$ of the four-core spiral chimera with $w(x, y) = w_p(x, y)$ defined in Section 3.1. This means that the zeros of Eq. (38) coincide with those of Eq. (30) and so appear for identical parameter values (β, γ) . Thus every solution to Eq. (38) is a multiplicity-two real eigenvalue, this time with the eigenvectors shown in Figure 14 (top row). The resulting bifurcation $\lambda = 0$ is a parity-breaking bifurcation and takes place along the straight line $\beta = \beta_0 \approx 0.34$ (Figure 2).

4 Discussion and Conclusion

In this paper we have carried out a detailed analysis of the stability properties of four-core spiral chimera states present in the system (1)–(2) with periodic boundary conditions in the plane, following earlier work by Xie et al [29]. These four-core states are expected because the coupling function used, Eq. (2), has D_4 -symmetry. We have performed a detailed two-parameter stability analysis of the D_4 -symmetric state in the (β, γ) plane using the linearization of the Ott–Antonsen equation valid in the continuum limit. The stability analysis showed that this state can either lose stability at a parity-breaking bifurcation or via a Hopf bifurcation. The results are summarized in the stability diagram in Figure 2. We used numerical integration of the system (1)–(2) to study the evolution of each of the instabilities identified by the linear stability analysis. The results led to the discovery of quasiperiodic four-core chimera states, characterized by a coherent filament or filaments that rotate about an incoherent core with a new frequency. We have shown that these states are responsible for the discontinuous time-averaged order parameter profile noticed by Xie et al [29]. Our work shows explicitly how the properties of this profile relate to the number and termination of the coherent filaments present in this regime and describes the sequence of transitions that take place as β increases whereby the incoherent cores gradually shrink, leading to a four-core state with no incoherence within the cores.

Our work also identified a parity-breaking bifurcation as a second mechanism whereby the four-core chimera state can lose stability, but numerical simulations showed that the expected steadily drifting states were not in fact stable. These simulations did show, however, that the D_4 -symmetric chimera

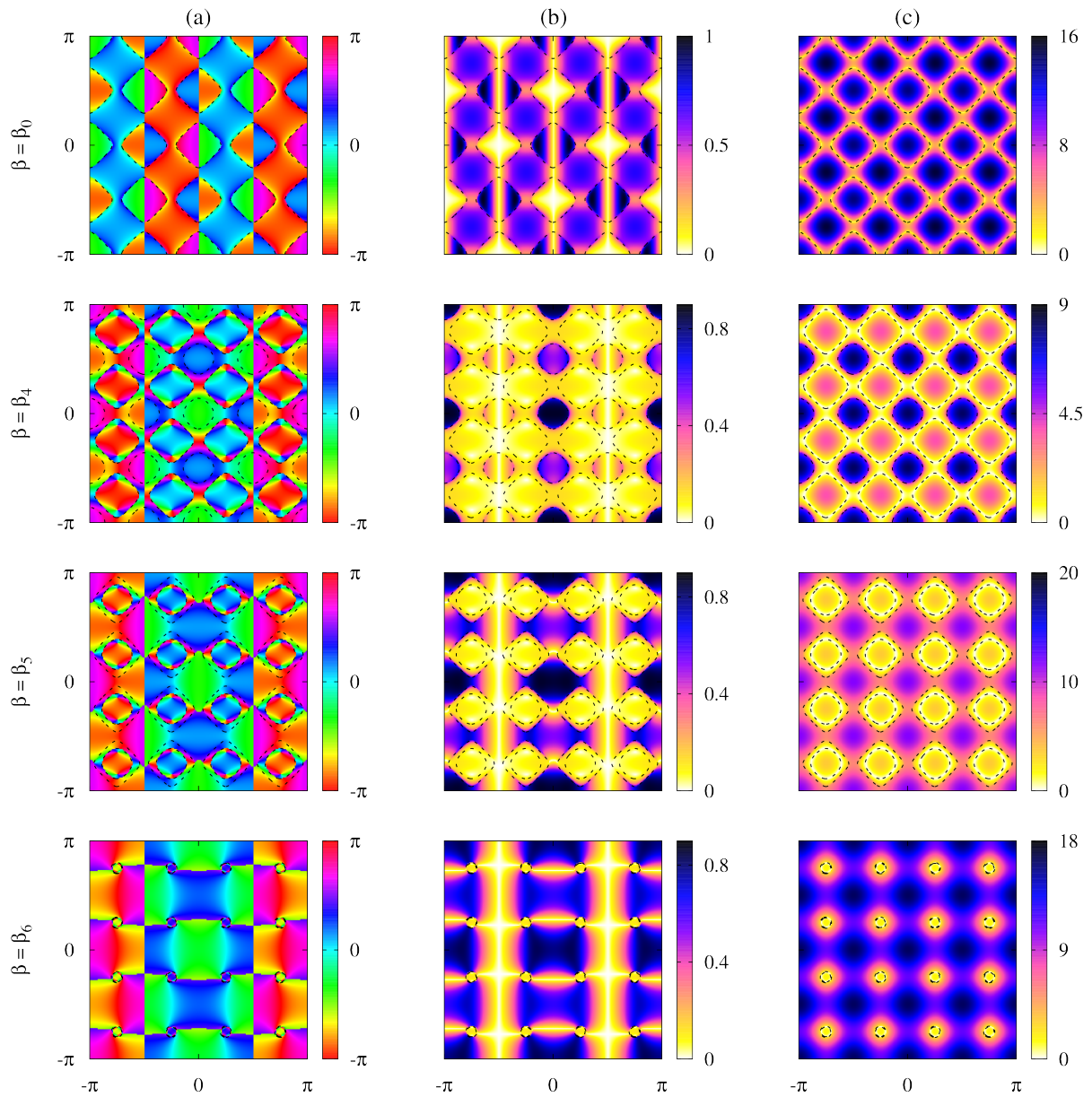


Figure 14: Marginal eigenmodes $v(x, y, 0)$ determined by expression (17) for 16-core basic chimera spiral at the four bifurcation points $\beta = \beta_0, \beta_4, \beta_5, \beta_6$ and $\gamma = 0.63$. Columns (a), (b) and (c) show $\arg v(x, y)$, $|(\lambda_{\text{cr}} + \Omega(|w(x, y)|^2))v(x, y)|$ and $|\lambda_{\text{cr}} + \Omega(|w(x, y)|^2)|$, respectively, where λ_{cr} denotes the critical eigenvalue at the corresponding bifurcation point. Dashed lines show position of the coherence-incoherence boundary and of the singularity contour.

state coexists with a number of additional states. Of these we focused here on a D_2 -symmetric four-core chimera state and a 16-core chimera state. For each of these states we carried out a similar linear stability analysis the results of which are also summarized in Figure 2.

These stability calculations form the highlight of this work (some key technical advances are summarized in Appendices A and B) and open the subject of spiral chimera states to the techniques of bifurcation analysis [19, 20]. Our results also point to the need for a clearer mathematical understanding of the role played by the singular contour $|w_p(x, y)|^2 = 1 - (\omega_p/\Omega)^2$ (Eq. (33)) in determining the origin of the coherent filaments that appear whenever the state loses stability via a Hopf bifurcation and their interaction with the coherence-incoherence boundary (Eq. (29)).

Appendix A: Characteristic equations (30) and (31) for symmetric four-core spirals

Each element of the matrix $B(\lambda)$ is defined as a double integral, therefore numerical solution of the characteristic equation (28) turns out to be an extremely time-consuming process. In this section we show that after an appropriate coordinate transformation these double integrals can be analytically integrated with respect to one variable and thus significantly simplified. This allows us to increase the speed of all numerical routines by several orders of magnitude without loss of accuracy.

First, we recall the standard definition of the complete elliptic integral of the first and the second kinds

$$K(m) = \int_0^{\pi/2} \frac{d\varphi}{\sqrt{1 - m \sin^2 \varphi}}, \quad E(m) = \int_0^{\pi/2} \sqrt{1 - m \sin^2 \varphi} d\varphi, \quad \text{where } m \in [0, 1]. \quad (39)$$

These integrals cannot be expressed in terms of elementary functions, but they are usually implemented as standard functions in most programming languages (*C/C++*, *FORTRAN* etc) and mathematical computing environments (*MATLAB*, *Mathematica* etc).

We explain the coordinate transformation approach for the self-consistency equation (8).

Proposition 2 Equation (8) can be rewritten in the form

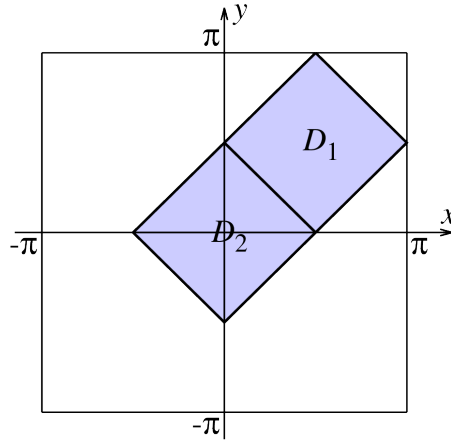
$$\mu = 8 \int_0^1 \left(h(p^2(2-s)) - \frac{s}{s-2} h(p^2 s) \right) K \left(\frac{s^2}{(s-2)^2} \right) ds. \quad (40)$$

Proof: Substituting expression (10) into Eq. (8) and taking into account the obvious identity

$$\int_{-\pi}^{\pi} dx \int_{-\pi}^{\pi} h(p^2(\cos^2 x + \cos^2 y)) \cos x \cos y dy = 0$$

we obtain

$$\begin{aligned} \mu &= \int_{-\pi}^{\pi} \int_{-\pi}^{\pi} h(p^2(\cos^2 x + \cos^2 y)) \cos^2 x dx dy \\ &= \frac{1}{2} \int_{-\pi}^{\pi} \int_{-\pi}^{\pi} h(p^2(\cos^2 x + \cos^2 y)) (\cos^2 x + \cos^2 y) dx dy. \end{aligned}$$

Figure 15: Etalon domain $D_1 \cup D_2$.

Using the symmetries of the integrand we can replace the integration domain $[-\pi, \pi]^2$ with another domain consisting of the two squares D_1 and D_2 shown in Figure 15. This yields

$$\mu = 2 \iint_{D_1 \cup D_2} h(p^2(\cos^2 x + \cos^2 y)) (\cos^2 x + \cos^2 y) dx dy.$$

In the square D_1 we rewrite the integrand using modified polar coordinates

$$\begin{cases} x = \arccos(q \cos t), \\ y = \arccos(q \sin t), \end{cases} \quad (41)$$

with new variables $(q, t) \in [0, 1] \times [0, 2\pi]$. The Jacobian of this transformation reads

$$J(q, t) = \frac{\partial x}{\partial q} \frac{\partial y}{\partial t} - \frac{\partial x}{\partial t} \frac{\partial y}{\partial q} = \frac{2q}{\sqrt{4(1-q^2) + q^4 \sin^2 2t}}. \quad (42)$$

In the square D_2 we rewrite the integrand applying a slightly different coordinate transformation,

$$\begin{cases} x = \arcsin(q \cos t), \\ y = \arcsin(q \sin t), \end{cases} \quad (43)$$

which turns out to have the same Jacobian as in Eq. (42). Altogether we obtain

$$\begin{aligned} \mu &= 2 \int_0^1 dq \int_0^{2\pi} \frac{h(p^2 q^2) q^2 \cdot 2q}{\sqrt{4 - 4q^2 + q^4 \sin^2 2t}} + 2 \int_0^1 dq \int_0^{2\pi} \frac{h(p^2(2-q^2))(2-q^2) \cdot 2q}{\sqrt{4 - 4q^2 + q^4 \sin^2 2t}} \\ &= 2 \int_0^1 ds \int_0^{2\pi} \frac{h(p^2 s)s + h(p^2(2-s))(2-s)}{\sqrt{4 - 4s + s^2 \sin^2 2t}} dt \\ &= 8 \int_0^1 ds (h(p^2 s)s + h(p^2(2-s))(2-s)) \int_0^{\pi/2} \frac{d\varphi}{\sqrt{4 - 4s + s^2 \sin^2 \varphi}}. \end{aligned}$$

The integral with respect to φ can be expressed in terms of the complete elliptic integrals (39) and we obtain the desired formula (40). ■

We next show that the elements of the matrices appearing in the characteristic equations (30) and (31) can all be expressed in terms of just five independent functions. For the sake of brevity we introduce the notation

$$M_p(s, \lambda) := (\lambda + \Omega_p \eta(s))^{-1} \quad \text{and} \quad N_p(s, \lambda) := (\lambda + \Omega_p \eta(s))^{-1} h^2(s) p^2,$$

where the functions $h(s)$ and $\eta(s)$ are defined in Eqs. (6) and (15). The index p in Ω_p (and also in α_p below) indicates that parameters p , Ω and α are functionally dependent, namely they satisfy the self-consistency equation (40) with $\mu = i\Omega e^{i\alpha}$.

Recalling that $\psi_3(x) = \cos 2x$, $\psi_4(x) = \cos 2y$ and using the expressions

$$\begin{aligned} |w_p(x, y)|^2 &= p^2(\cos^2 x + \cos^2 y), \\ a_p^2(x, y) &= h^2(|w_p(x, y)|^2) w_p^2(x, y) \\ &= h^2(p^2(\cos^2 x + \cos^2 y)) p^2(\cos^2 x - \cos^2 y + 2i \cos x \cos y), \end{aligned}$$

which follow from Eqs. (5) and (10), we obtain

$$\begin{pmatrix} B_{33}(\lambda) & B_{34}(\lambda) \\ B_{43}(\lambda) & B_{44}(\lambda) \end{pmatrix} = \begin{pmatrix} A_1(\lambda, p) & A_2(\lambda, p) & A_3(\lambda, p) & 0 \\ \overline{A_2(\bar{\lambda}, p)} & \overline{A_1(\bar{\lambda}, p)} & 0 & \overline{A_3(\bar{\lambda}, p)} \\ A_3(\lambda, p) & 0 & A_1(\lambda, p) & -A_2(\lambda, p) \\ 0 & \overline{A_3(\bar{\lambda}, p)} & -\overline{A_2(\bar{\lambda}, p)} & \overline{A_1(\bar{\lambda}, p)} \end{pmatrix}, \quad (44)$$

where

$$\begin{aligned} A_1(\lambda, p) &= e^{-i\alpha_p} \left\langle (\lambda + \Omega_p \eta(|w_p|^2))^{-1} \psi_3^2 \right\rangle = e^{-i\alpha_p} \left\langle (\lambda + \Omega_p \eta(|w_p|^2))^{-1} \psi_4^2 \right\rangle \\ &= \frac{1}{2} e^{-i\alpha_p} \left\langle M_p(p^2(\cos^2 x + \cos^2 y), \lambda) (\cos^2 2x + \cos^2 2y) \right\rangle, \\ A_2(\lambda, p) &= e^{-i\alpha_p} \left\langle (\lambda + \Omega_p \eta(|w_p|^2))^{-1} a_p^2 \psi_3^2 \right\rangle = -e^{-i\alpha_p} \left\langle (\lambda + \Omega_p \eta(|w_p|^2))^{-1} a_p^2 \psi_4^2 \right\rangle \\ &= \frac{1}{2} e^{-i\alpha_p} \left\langle N_p(p^2(\cos^2 x + \cos^2 y), \lambda) (\cos^2 x - \cos^2 y)(\cos^2 2x - \cos^2 2y) \right\rangle, \\ A_3(\lambda, p) &= e^{-i\alpha_p} \left\langle (\lambda + \Omega_p \eta(|w_p|^2))^{-1} \psi_3 \psi_4 \right\rangle \\ &= e^{-i\alpha_p} \left\langle M_p(p^2(\cos^2 x + \cos^2 y), \lambda) \cos 2x \cos 2y \right\rangle. \end{aligned}$$

The anti-diagonal elements on the right-hand side of Eq. (44) vanish because for any continuous function $f : [0, 1]^2 \rightarrow \mathbb{R}$ we have

$$\int_{-\pi}^{\pi} f(\cos^2 x, \cos^2 y) \cos x \, dx = \int_{-\pi}^{\pi} f(\cos^2 x, \cos^2 y) \cos y \, dy = 0.$$

The same identity also explains the absence of the term proportional to

$$\left\langle N_p(p^2(\cos^2 x + \cos^2 y), \lambda) \cos x \cos y (\cos^2 2x - \cos^2 2y) \right\rangle$$

on the right side of the expression for $A_2(\lambda, p)$.

Similarly, using the definition $\psi_5(x) = \sin x$ and the explicit form of the functions w_p and a_p , we rewrite the matrix $B_{55}(\lambda)$ from Eq. (30) in the form

$$B_{55}(\lambda) = \begin{pmatrix} A_4(\lambda, p) & A_5(\lambda, p) \\ A_5(\bar{\lambda}, p) & A_4(\bar{\lambda}, p) \end{pmatrix}, \quad (45)$$

where

$$\begin{aligned} A_4(\lambda, p) &= e^{-i\alpha_p} \left\langle (\lambda + \Omega_p \eta (|w_p|^2))^{-1} \psi_5^2 \right\rangle \\ &= \frac{1}{2} e^{-i\alpha_p} \left\langle M_p(p^2(\cos^2 x + \cos^2 y), \lambda) (\sin^2 x + \sin^2 y) \right\rangle, \\ A_5(\lambda, p) &= e^{-i\alpha_p} \left\langle (\lambda + \Omega_p \eta (|w_p|^2))^{-1} a_p^2 \psi_3^2 \right\rangle \\ &= \frac{1}{2} e^{-i\alpha_p} \left\langle N_p(p^2(\cos^2 x + \cos^2 y), \lambda) (\cos^2 x - \cos^2 y)(\sin^2 x - \sin^2 y) \right\rangle \\ &= -\frac{1}{2} e^{-i\alpha_p} \left\langle N_p(p^2(\cos^2 x + \cos^2 y), \lambda) (\cos^2 x - \cos^2 y)^2 \right\rangle. \end{aligned}$$

The coordinate transformation approach described in the proof of Proposition 2 can again be used to simplify the double integrals in the definition of the functions $A_k(\lambda, p)$, $k = 1, \dots, 5$. This yields

$$\begin{aligned} A_1(\lambda, p) &= 16e^{-i\alpha_p} \int_0^1 \left(M_p(p^2 s, \lambda) + M_p(p^2(2-s), \lambda) \right) \\ &\quad \times \left((s-2)E\left(\frac{s^2}{(s-2)^2}\right) - \frac{2s^2-6s+5}{s-2} K\left(\frac{s^2}{(s-2)^2}\right) \right) ds, \quad (46) \end{aligned}$$

$$\begin{aligned} A_2(\lambda, p) &= 32e^{-i\alpha_p} \int_0^1 \left(N_p(p^2 s, \lambda) - N_p(p^2(2-s), \lambda) \right) \\ &\quad \times (s-1)(s-2) \left(E\left(\frac{s^2}{(s-2)^2}\right) - K\left(\frac{s^2}{(s-2)^2}\right) \right) ds, \quad (47) \end{aligned}$$

$$\begin{aligned} A_3(\lambda, p) &= -16e^{-i\alpha_p} \int_0^1 \left(M_p(p^2 s, \lambda) + M_p(p^2(2-s), \lambda) \right) \\ &\quad \times \left((s-2)E\left(\frac{s^2}{(s-2)^2}\right) + \frac{2s-3}{s-2} K\left(\frac{s^2}{(s-2)^2}\right) \right) ds, \quad (48) \end{aligned}$$

$$A_4(\lambda, p) = -8e^{-i\alpha_p} \int_0^1 \frac{M_p(p^2 s, \lambda)(2-s) + M_p(p^2(2-s), \lambda)s}{s-2} K\left(\frac{s^2}{(s-2)^2}\right) ds, \quad (49)$$

$$\begin{aligned} A_5(\lambda, p) &= 8e^{-i\alpha_p} \int_0^1 \left(N_p(p^2 s, \lambda) + N_p(p^2(2-s), \lambda) \right) \\ &\quad \times (s-2) \left(E\left(\frac{s^2}{(s-2)^2}\right) - K\left(\frac{s^2}{(s-2)^2}\right) \right) ds. \quad (50) \end{aligned}$$

Computing the functions $A_k(\lambda, p)$ from the formulas (46)–(50) significantly accelerates our numerical routine for solving the nonlinear characteristic equations (30) and (31) obtained from Eqs. (44) and (45).

Appendix B: Characteristic equations (37) for symmetric 16-core spirals

Applying the procedure used above for the four-core spiral state leads to the following form of the self-consistency equation for the 16-core spiral state:

$$\mu = 8\gamma \int_0^1 \left(h(p^2(2-s)) - \frac{s}{s-2} h(p^2s) \right) K \left(\frac{s^2}{(s-2)^2} \right) ds.$$

The characteristic equation describing the lower stability boundary of this state (red curve in Figure 2) can likewise be written in simpler form. This instability arises from the block

$$B_{11}(\lambda) = \begin{pmatrix} A_6(\lambda, p) & A_7(\lambda, p) \\ \frac{A_6(\bar{\lambda}, p)}{A_7(\bar{\lambda}, p)} & \frac{A_7(\bar{\lambda}, p)}{A_6(\bar{\lambda}, p)} \end{pmatrix}, \quad (51)$$

where

$$\begin{aligned} A_6(\lambda, p) &= e^{-i\alpha p} \left\langle (\lambda + \Omega_p \eta (|W_p|^2))^{-1} \psi_1^2 \right\rangle \\ &= \frac{1}{2} e^{-i\alpha p} \left\langle M_p(p^2(\cos^2 2x + \cos^2 2y), \lambda) (\cos^2 x + \cos^2 y) \right\rangle, \\ &= -8e^{-i\alpha p} \int_0^1 \frac{M_p(p^2s, \lambda) + M_p(p^2(2-s), \lambda)}{s-2} K \left(\frac{s^2}{(s-2)^2} \right) ds, \\ A_7(\lambda, p) &= e^{-i\alpha p} \left\langle (\lambda + \Omega_p \eta (|W_p|^2))^{-1} a_p^2 \psi_1^2 \right\rangle \\ &= \frac{1}{2} e^{-i\alpha p} \left\langle N_p(p^2(\cos^2 2x + \cos^2 2y), \lambda) (\cos^2 2x - \cos^2 2y)(\cos^2 x - \cos^2 y) \right\rangle \\ &= -\frac{1}{4} e^{-i\alpha p} \left\langle N_p(p^2(\cos^2 x + \cos^2 y), \lambda) (\cos^2 2x - \cos^2 2y)(\cos 2x - \cos 2y) \right\rangle \\ &= 0. \end{aligned}$$

The characteristic equation can thus be rewritten in the form

$$\det \left(I_2 - \frac{1}{2} B_{11}(\lambda) \right) = \left(1 - \frac{1}{2} A_6(\lambda, p) \right) \left(1 - \frac{1}{2} \overline{A_6(\bar{\lambda}, p)} \right) = 0.$$

References

- [1] D.M. Abrams and S.H. Strogatz, “Chimera states for coupled oscillators”, *Phys. Rev. Lett.* **93**, p. 174102 (2004).
- [2] P. Chossat and M. Golubitsky, “Symmetry-increasing bifurcation of chaotic attractors”, *Physica D* **32**, pp. 423–436 (1988).
- [3] C. Gu, G. St-Yves, and J. Davidsen, “Spiral wave chimeras in complex oscillatory and chaotic systems”, *Phys. Rev. Lett.* **111**, p. 134101 (2013).

- [4] A. M. Hagerstrom, T. E. Murphy, R. Roy, P. Hövel, I. Omelchenko, and E. Schöll, "Experimental observation of chimeras in coupled-map lattices", *Nature Phys.* **8**, pp. 658–661 (2012).
- [5] T. Kapitaniak, P. Kuzma, J. Wojewoda, K. Czolczynski, and Y. Maistrenko, "Imperfect chimera states for coupled pendula", *Sci. Rep.* **4**, p. 6379 (2014).
- [6] P.-J. Kim, T.-W. Ko, H. Jeong, and H.-T. Moon, "Pattern formation in a two-dimensional array of oscillators with phase-shifted coupling", *Phys. Rev. E* **70**, p. 065201 (2004).
- [7] Y. Kuramoto and D. Battogtokh, "Coexistence of coherence and incoherence in nonlocally coupled phase oscillators", *Nonlinear Phenom. Complex Syst.* **5**, pp. 380–385 (2002).
- [8] Y. Kuramoto and S. Shima, "Rotating spirals without phase singularity in reaction-diffusion systems", *Prog. Theor. Phys. Suppl.* **150**, pp. 115–125 (2003).
- [9] C. Laing, "The dynamics of chimera states in heterogeneous Kuramoto networks", *Physica D* **238**, pp. 1569–1588 (2009).
- [10] C. Laing, "Chimeras in two-dimensional domains: heterogeneity and the continuum limit", *SIAM Journal on Applied Dynamical Systems* **16**, pp. 974–1014 (2017)
- [11] H. W. Lau and J. Davidsen, "Linked and knotted chimera filaments in oscillatory systems", *Phys. Rev. E* **94** p. 010204 (2016).
- [12] B.-W. Li and H. Dierckx, "Spiral wave chimeras in locally coupled oscillator systems", *Phys. Rev. E* **93**, p. 020202 (2016).
- [13] Y. Maistrenko, O. Sudakov, O. Osiv, and V. Maistrenko, "Chimera states in three dimensions", *New Journal of Physics* **17**, p. 073037 (2015).
- [14] E. A. Martens, C. R. Laing, and S. H. Strogatz, "Solvable model of spiral wave chimeras", *Phys. Rev. Lett.* **104**, p. 044101 (2010).
- [15] E. A. Martens, S. Thutupalli, A. Fourriere, and O. Hallatschek, "Chimera states in mechanical oscillator networks", *Proc. Natl Acad. Sci. USA* **110**, p. 10563–10567 (2013).
- [16] S. Nkomo, M. R. Tinsley, and K. Showalter, "Chimera States in Populations of Nonlocally Coupled Chemical Oscillators", *Phys. Rev. Lett.* **110**, p. 244102 (2013).
- [17] O. E. Omel'chenko, M. Wolfrum, S. Yanchuk, Y. L. Maistrenko, and O. Sudakov, "Stationary patterns of coherence and incoherence in two-dimensional arrays of non-locally coupled phase oscillators", *Phys. Rev. E* **85**, p. 036210 (2012).
- [18] O. E. Omel'chenko, M. Wolfrum, and Y. L. Maistrenko, "Chimera states as chaotic spatio-temporal patterns", *Phys. Rev. E* **81**, p. 065201 (2010).
- [19] O. E. Omel'chenko, "Coherence-incoherence patterns in a ring of non-locally coupled phase oscillators", *Nonlinearity* **26**, pp. 2469–2498 (2013).
- [20] O. E. Omel'chenko, "The mathematics behind chimera states", *Nonlinearity* **30** (2017).
- [21] E. Ott and T. M. Antonsen, "Low dimensional behavior of large systems of globally coupled oscillators", *Chaos* **18**, p. 037113 (2008).

- [22] E. Ott and T. M. Antonsen, “Long time evolution of phase oscillator systems ”, *Chaos* **19**, p. 023117 (2009).
- [23] M. J. Panaggio and D. M. Abrams, “Chimera states on a flat torus”, *Phys. Rev. Lett.* **110**, p. 094102 (2013).
- [24] M. J. Panaggio and D. M. Abrams, “Chimera states: coexistence of coherence and incoherence in networks of coupled oscillators”, *Nonlinearity* **28**, pp. R67–R87 (2015).
- [25] M. J. Panaggio and D. M. Abrams, “Chimera states on the surface of a sphere”, *Phys. Rev. E* **91**, p. 022909 (2015).
- [26] S. Shima and Y. Kuramoto, “Rotating spiral waves with phase-randomized core in nonlocally coupled oscillators”, *Phys. Rev. E* **69**, p. 036213 (2004).
- [27] M. R. Tinsley, S. Nkomo, and K. Showalter, “Chimera and phase-cluster states in populations of coupled chemical oscillators”, *Nature Phys.* **8**, pp. 662–665 (2012).
- [28] J. Xie, E. Knobloch, and H.-C. Kao, “Multiclustler and traveling chimera states in nonlocal phase-coupled oscillators”, *Phys. Rev. E* **90**, p. 022919 (2014).
- [29] J. Xie, E. Knobloch, and H.-C. Kao, “Twisted chimera states and multicore spiral chimera states on a two-dimensional torus”, *Phys. Rev. E* **92**, p. 042921 (2015).